

Cite this: *Mater. Horiz.*, 2025, 12, 4724Received 14th February 2025,  
Accepted 26th March 2025

DOI: 10.1039/d5mh00272a

rsc.li/materials-horizons

# Constructing a biomimetic TiOF<sub>2</sub>@PCN-222-Fe Z-scheme heterojunction using self-assembled L-cysteine for CO<sub>2</sub> visible light photoreduction†

Yi Ping,<sup>a</sup> Chuanjiao Wang,<sup>a</sup> Changan Hou,<sup>a</sup> Zhenfeng Shang<sup>b</sup> and Danhong Wang<sup>ib</sup>\*<sup>a</sup>

Biomimetic synthesis via MOF-based catalysts to construct a Z-scheme heterojunction provides opportunities for enhancement of visible light photocatalytic CO<sub>2</sub> reduction efficiency. Herein, a TiOF<sub>2</sub>@PCN-222-Fe heterojunction was designed using the L-cysteine agglomerant to simulate the structure of cytochrome *c* oxidase. L-cysteine axially coordinated with Fe<sup>3+</sup> in the ferroporphyrin moiety of PCN-222-Fe through the –SH group and coordinated with Ti<sup>4+</sup> in TiOF<sub>2</sub> through the –COOH group. This heterojunction enhances photocurrent and conductivity, thus improving CO<sub>2</sub> visible light photocatalytic activity. Various characterization methods including EXAFS and theoretical calculations demonstrated that the band bending of TiOF<sub>2</sub> and PCN-222-Fe occurred through L-cysteine coordination and a Z-scheme heterojunction was formed to efficiently separate photogenerated carriers. Thus, TiOF<sub>2</sub> accumulates electrons and acts as the active center of CO<sub>2</sub> reduction, PCN-222-Fe accumulates holes and acts as the active center of water oxidation, and L-cysteine provides the transmission pathway of protons. The introduction of F element in TiOF<sub>2</sub> lowered the valence band, which produced energetic holes that transferred to the valence band of PCN-222-Fe for water oxidation. This strategy provides unique insights into improving the efficiency of CO<sub>2</sub> visible light photoreduction by biomimetic design of Z-scheme heterojunctions.

## 1. Introduction

In recent years, the energy crisis and environmental problems caused by the rapid consumption of fossil fuels have attracted much attention. Excessive CO<sub>2</sub><sup>1</sup> emissions negatively affect many aspects of life, including accelerating global warming,

### New concepts

In this study, a TiOF<sub>2</sub>@PCN-222-Fe heterojunction was synthesized with L-cysteine as a bridging agent to mimic cytochrome *c* oxidase. L-cysteine coordinates with Fe<sup>3+</sup> in PCN-222-Fe via its –SH group and with Ti<sup>4+</sup> in TiOF<sub>2</sub> through its –COOH group. This configuration enhances photocurrent, electrical conductivity, and photocatalytic CO<sub>2</sub> reduction under visible light. EXAFS and theoretical calculations show that L-cysteine induces band bending, forming a Z-scheme heterojunction that separates charge carriers effectively. TiOF<sub>2</sub> accumulates electrons for CO<sub>2</sub> reduction, while PCN-222-Fe accumulates holes for water oxidation. L-cysteine also aids proton transport. Fluorine in TiOF<sub>2</sub> lowers the valence band, creating high-energy holes that migrate to PCN-222-Fe, driving water oxidation. This biomimetic Z-scheme design provides a novel strategy for improving visible light-driven CO<sub>2</sub> photoreduction efficiency.

ocean acidification, reducing crop yields, extinction of animal species, and damage to human health.<sup>2</sup> With CO<sub>2</sub> concentrations already as high as 420 ppm in air,<sup>3</sup> reducing the CO<sub>2</sub> concentration in air, especially by using solar energy to convert CO<sub>2</sub><sup>4,5</sup> into fuel or value-added chemicals, is a promising approach.<sup>6</sup>

Metal-organic frameworks (MOFs) are a class of porous crystal materials with high surface area and adjustable pore size<sup>7,8</sup> and have great potential in applications such as gas storage, sensing, and catalysis.<sup>9</sup> In 2020, Prof. Lin and his team reported that mPT-Cu/Co and mPT-Cu/Re, the two multifunctional metal-organic frameworks, showed significantly enhanced photocatalytic activity for photocatalytic hydrogen production and CO<sub>2</sub> reduction by integrating Cu-PSS and Co/Re catalysts in MOFs, with an HER TON of 18 700 for mPT-Cu/Co and a CO<sub>2</sub>RR TON of 1328 for mPT-Cu/Re.<sup>10</sup> Recent results showed that NNU-13 had a very high selectivity of >96% for the photocatalytic reduction of CO<sub>2</sub> to CH<sub>4</sub> in combination with polyacid-based metal coordination frameworks (POMCF compounds NNU-13 and NNU-14) in H<sub>2</sub>O/TEOA (14 : 1 v/v, 30 mL).<sup>11</sup> In addition, PCN-222 is formed by the coordination of the porphyrin tetracarboxylic acid ligand (TCPP) and Zr<sub>6</sub> clusters.

<sup>a</sup>TKL of Metal and Molecule Based Material Chemistry, School of Materials Science and Engineering, Nankai University, Tianjin 300350, China.

E-mail: dhwang@nankai.edu.cn

<sup>b</sup>Frontiers Science Center for New Organic Matter, College of Chemistry, Nankai University, Tianjin 300071, China

† Electronic supplementary information (ESI) available. See DOI: <https://doi.org/10.1039/d5mh00272a>

Each  $Zr_6(OH)_8$  core, in which all triangular faces in the  $Zr_6$ -octahedron are covered by  $\mu_3$ -OH groups, is attached to eight TCPP ligands. The symmetry of the  $Zr_6$  carboxylate unit is reduced from  $O_h$  to  $D_{4h}$ , which may create a surplus space for the formation of the mesopores. The benzene ring of the TCPP ligand is also rotated  $35.88^\circ$  from the original position corresponding to that in the free ligand.<sup>12</sup> The 3D framework of PCN-222 can also be seen as zirconium-carboxylate layers, which form a Kagome-type pattern in the  $ab$  plane, linked by TCPP ligands.<sup>12</sup> The rigid planar conjugated structure of porphyrinyl MOF catalysts can improve light absorption and electron transport capacity.<sup>13</sup> Since heme can normally catalyze various reactions in aqueous solution, in 2012, Zhou's group<sup>12</sup> used highly stable  $Zr_6$  clusters as nodes and Fe-TCPP as a heme organic ligand to construct a three-dimensional heme PCN-222(Fe) with a pore size of 3.7 nm, which contains one of the largest known one-dimensional open channels. At the same time, a series of MOFs with the same topology were prepared by replacing Fe with other metals, defined as PCN-222-M (M = Zr, Mn, Co, Ni, Cu, Zn).

As a commonly used semiconductor photocatalyst,  $TiO_2$ <sup>14</sup> has the characteristics of non-toxicity, low price and good chemical stability.<sup>15,16</sup> However, its wide energy bandgap<sup>17</sup> and high carrier recombination<sup>18</sup> rate hinder its application in photocatalysis.<sup>19</sup> The introduction of F element can enhance the electronic conductivity and lower the valence band due to the electron withdrawing effect of F, thus improving the photocatalytic activity.  $TiOF_2$  has a cubic  $ReO_3$  type structure (perovskite structure), which can be obtained by the commonly used solvothermal method based on the random distribution of O and F anions in the shared  $TiO_2F_4$  octahedron (Fig. 1). Due to the above advantages,  $TiOF_2$  can be applied in the field of

photocatalysis.<sup>20</sup> Wang *et al.*<sup>21</sup> prepared the  $TiOF_2$  photocatalyst for decomposing rhodamine B and 4-chlorophenol under visible light, which showed certain photocatalytic activity and stability, but the photocatalytic performance was still unsatisfactory. Dong *et al.*<sup>22</sup> synthesized  $Ag_3PO_4/TiOF_2$  hetero-semiconductor composites to improve the photocatalytic activity and stability of  $Ag_3PO_4$ .

L-cysteine<sup>23</sup> is an important regulator often used in the synthesis of biomimetic<sup>24,25</sup> materials. The sulfhydryl group in L-cysteine is easily deprotonated and coordinated with metal ions to form active functional groups, which can regulate many aspects of the biomimetic photocatalysts, including the transmission of electrons and protons for biomimetic reaction mechanisms.<sup>26</sup> For example, Wu *et al.* recombined L-cysteine with gold nanoparticles to form Au-S covalent bonds, which facilitate electrochemical reactions.<sup>27</sup> In the composite fabrication process of the raw materials, the different coordination abilities of -SH and -COOH groups in L-cysteine can lead to orderly ligation, thus effectively controlling the self-assembly orientation of the raw materials. However, studies on the interaction between L-cysteine and the raw materials for  $CO_2$  photocatalytic reduction are rarely reported.

Nature relies on the iron porphyrin site in heme to activate and reduce oxygen.<sup>28,29</sup> In particular, the reduction of oxygen to water through cytochrome *c* oxidase is an important process during the respiratory activities of organisms. At present, nickel,<sup>30-32</sup> cobalt,<sup>33,34</sup> and copper<sup>35</sup> porphyrin complexes have been found to catalyze oxygen evolution reactions and have good catalytic activity. However, the reaction mechanism of iron porphyrins for oxygen evolution reactions has not been clearly studied. Since the  $CO_2$  reduction reaction is the other half of the oxygen evolution reaction, it is speculated that an

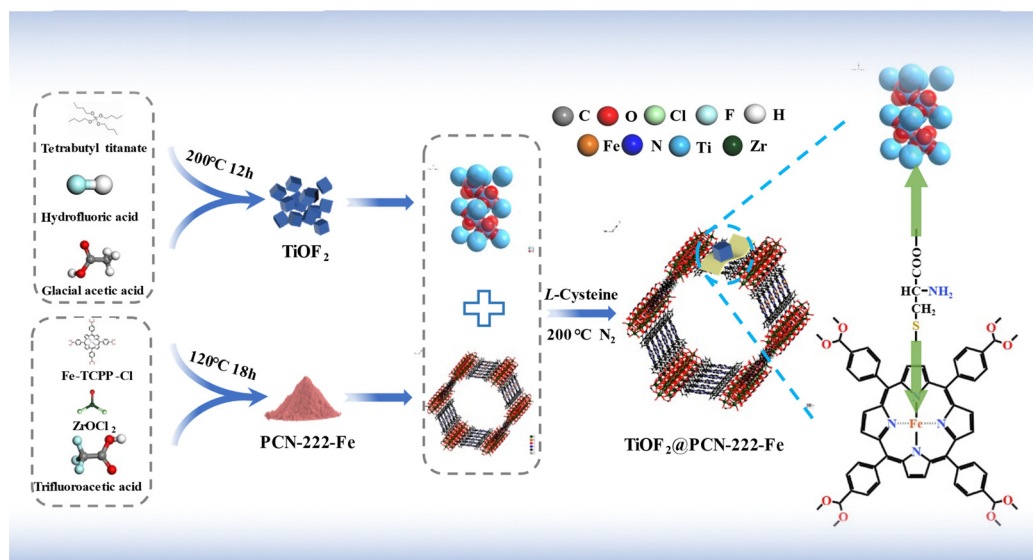


**Fig. 1** Schematic diagram of the  $TiOF_2@PCN-222-Fe$  composite. The dark gray, red, green, blue-green, white, orange, dark blue, sky blue, and dark gray balls represent carbon, oxygen, chlorine, fluorine, hydrogen, iron, nitrogen, titanium, and zirconium, respectively. In particular, the red ball in  $TiOF_2$  represents the element fluorine or oxygen. The green arrows indicate that the sulfhydryl group in L-cysteine is linked to iron in PCN-222-Fe, and the carboxyl group is linked to O/F in  $TiOF_2$ .

iron porphyrin molecular catalyst with both CO<sub>2</sub> reduction and oxygen evolution activities can be obtained by rationally designing the structure of iron porphyrins. In this work, inspired by nature, an enzyme-like iron porphyrin complex (Fig. 1) was designed, which successfully mimicked the iron porphyrin center of cytochrome *c* oxidase, by molecular structure design with *L*-cysteine linkage to coordinate TiOF<sub>2</sub> in the iron porphyrin axis. It was found that by introducing the axial ligand in this enzyme-like composite, it was possible to achieve simultaneous and efficient catalysis of CO<sub>2</sub> reduction and oxygen precipitation. It is also one of the few molecular catalysts that can catalyze both oxygen reduction and oxygen evolution reactions. The transmission paths of electrons and protons in this enzyme-like composite for biomimetic reaction mechanisms were thus excluded.

## 2. Results and discussion

### 2.1. Characterization of morphology and structure

PCN-222-Fe with a formula of C<sub>96</sub>H<sub>64</sub>Cl<sub>2</sub>Fe<sub>2</sub>N<sub>8</sub>O<sub>32</sub>Zr<sub>6</sub>, composed of one mole of the Zr<sub>6</sub>O<sub>8</sub>(μ<sub>3</sub>-OH)<sub>8</sub> cluster and two moles of the 5,10,15,20-tetrakis-(4-carboxyphenyl)-porphyrin-Fe(III) chloride ligand (C<sub>48</sub>H<sub>28</sub>ClFeN<sub>4</sub>O<sub>8</sub>), was chosen as the model mesoporous framework with a diameter of 3.7 nm in the semiconductor heterojunction photocatalyst to act as the active site of the oxygen evolution reaction (OER). Nanoscale PCN-222-Fe particles were synthesized firstly as uniform shuttle-like nanocrystals with an average size of *ca.* 400 nm length and *ca.* 100 nm diameter, as demonstrated by transmission electron microscopy (TEM) and scanning electron microscopy (SEM) characterization methods (Fig. 2 and Fig. S1, ESI<sup>†</sup>). Titanium oxyfluoride was simply synthesized *via* the hydrothermal reaction of tetrabutyl titanate with hydrofluoric acid, which generated TiOF<sub>2</sub> nanocubes. The nanocubes with hexagonal TiOF<sub>2</sub> structure (space group *R*3*c*) consist of Ti atoms octahedrally coordinated by randomly distributed O and F atoms. The TiO<sub>2</sub>F<sub>4</sub> octahedra share all six corners with neighboring octahedra. Each unit cell contains six TiOF<sub>2</sub> molecules as shown in Fig. 1. The theoretical density and

Ti–O/F distances are 3.114 g cm<sup>-3</sup> and 1.911 Å, respectively. To incorporate TiOF<sub>2</sub> onto PCN-222-Fe *via* coordination, excess amounts of *L*-cysteine (100 mg) as an agglomerant to fully cover the surface of PCN-222-Fe were mixed with as-synthesized TiOF<sub>2</sub> (20 mg) and PCN-222-Fe nanoparticles (80 mg) in ethanol and stirred at 80 °C for 4 h. The resulting powder was calcined at 200 °C in a nitrogen atmosphere to remove unbound *L*-cysteine. The obtained TiOF<sub>2</sub>@PCN-222-Fe composite has a surface area of 26.2 m<sup>2</sup> g<sup>-1</sup>.

The morphology and microstructure of catalysts determined by SEM are showed in Fig. S1 (ESI<sup>†</sup>). It can be seen in the SEM image of the TiOF<sub>2</sub>@PCN-222-Fe composite that the regular cubic TiOF<sub>2</sub> nanoparticles are loaded onto the shuttle-like PCN-222-Fe particles. The side length of cubic TiOF<sub>2</sub> is about 100 nm, as shown in Fig. 2a, which is similar to the diameter of shuttle-like PCN-222-Fe (~100 nm), as shown in Fig. 2b. It is suggested from the theory of soft and hard acids and bases that the carboxyl group (–COOH) in *L*-cysteine is a hard base, the metal ions Ti<sup>4+</sup> with high valence in TiOF<sub>2</sub> should more easily coordinate with –COOH, and the sulfhydryl group –SH in *L*-cysteine is a soft base that prefers to combine with Fe<sup>3+</sup> with low valence in PCN-222-Fe. When PCN-222-Fe, TiOF<sub>2</sub> and *L*-cysteine were calcined together at 200 °C in a nitrogen atmosphere, the coordination of PCN-222-Fe with the sulfhydryl group and the coordination of TiOF<sub>2</sub> with the carboxyl group occurred; thus, PCN-222-Fe and TiOF<sub>2</sub> can be successfully combined through *L*-cysteine. On the other hand, the electronegativity is as follows: Ti 1.54, Fe 1.96, S 2.58, and O 3.44; hard acid Ti<sup>4+</sup> and hard base COO<sup>-</sup> have stronger Coulomb force to combine together. This supposition is confirmed by the subsequent characterization using FT-IR, XPS, UV-vis DRS and NMR. Since the TCPP-Fe ligand coordinates with TiOF<sub>2</sub> *via* *L*-cysteine, TiOF<sub>2</sub> nanocubes are uniformly spliced on the surface of shuttle-like PCN-222-Fe. In Fig. 2a and b, it can be seen that the lattice fringe of pure TiOF<sub>2</sub> is 2.67 Å, corresponding to the (110) facet, and that of pure PCN-222-Fe is 3.78 Å. In the TEM image shown in Fig. 2c for the TiOF<sub>2</sub>@PCN-222-Fe composite, the observed lattice fringe of TiOF<sub>2</sub> is 2.67 Å and that of PCN-222-Fe is 3.78 Å, which is the same as that before combination.

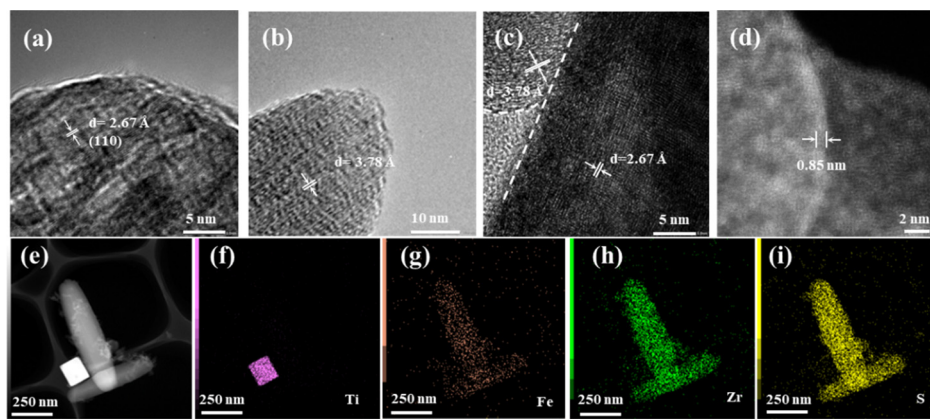


Fig. 2 TEM images of (a) TiOF<sub>2</sub>, (b) PCN-222-Fe, and (c) TiOF<sub>2</sub>@PCN-222-Fe, (d) spherical aberration-corrected TEM images of TiOF<sub>2</sub>@PCN-222-Fe, (e) TEM element mapping of TiOF<sub>2</sub>@PCN-222-Fe, (f) Ti, (g) Fe, (h) Zr, and (i) S.

In Fig. 2d, spherical aberration-corrected TEM images of the  $\text{TiOF}_2$ @PCN-222-Fe composite show that the surface of PCN-222-Fe is covered with L-cysteine and the thickness is about 0.85 nm, which is equal to the molecular length of L-cysteine. The chemical composition of the  $\text{TiOF}_2$ @PCN-222-Fe composite was determined by elemental mapping spectroscopy (Fig. 2e-i), and the results show that Fe and Zr are present uniformly in the shuttle-like PCN-222-Fe, and Ti mainly exists in the cubic  $\text{TiOF}_2$ . It is worth noting that S element in L-cysteine is mainly distributed on the surface of PCN-222-Fe, which is consistent with spherical aberration-corrected TEM results in Fig. 2d and also implies easy coordination of the sulfhydryl group with  $\text{Fe}^{3+}$  in TCPP-Fe. The distribution of these elements proved that PCN-222-Fe and  $\text{TiOF}_2$  were successfully combined through L-cysteine.

The nitrogen adsorption-desorption isotherms and pore size distribution curves of the catalysts are shown in Fig. S2 (ESI<sup>†</sup>). Pure  $\text{TiOF}_2$  shows a typical type II isotherm and has little pore volume (only  $0.004 \text{ cm}^3 \text{ g}^{-1}$ ) as shown in Table S1 (ESI<sup>†</sup>). The  $\text{TiOF}_2$ @PCN-222-Fe composites all show typical type IV isotherms, and all composites had hysteresis rings, indicating the mesoporous structure. The pore size of the  $\text{TiOF}_2$ @PCN-222-Fe composite analyzed *via* the BJH method is 2.2 nm, which is smaller than the calculated pore size of PCN-222-Fe (3.7 nm) as mentioned above. The BET surface area and pore volume of the samples are summarized in Table S1 (ESI<sup>†</sup>). The BET surface area of  $\text{TiOF}_2$  is only  $2.8 \text{ m}^2 \text{ g}^{-1}$ . However, the BET surface area of  $\text{TiOF}_2$ @PCN-222-Fe was increased to  $26.2 \text{ m}^2 \text{ g}^{-1}$ , indicating effective combination of  $\text{TiOF}_2$  and PCN-222-Fe. So it is inferred that the introduction of  $\text{TiOF}_2$  on PCN-222-Fe

was conducive to  $\text{CO}_2$  adsorption. The TGA curve in Fig. S3 (ESI<sup>†</sup>) shows that  $\text{TiOF}_2$  shows the lowest weight loss (28%) above  $500^\circ\text{C}$ , while PCN-222-Fe shows the highest weight loss (57%) above  $500^\circ\text{C}$ . The weight loss of the  $\text{TiOF}_2$ @PCN-222-Fe sample (52%) above  $500^\circ\text{C}$  is an intermediate between the two. The sudden weight loss of the composites  $\text{TiOF}_2$ @PCN-222,  $\text{TiOF}_2$ @PCN-222-Co and  $\text{TiOF}_2$ @PCN-222-Fe at  $240^\circ\text{C}$  was assigned to the decomposition of residual L-cysteine in the composites from the TGA curve of pure L-cysteine, although not shown here.

X-ray diffraction (XRD) analysis was used to study the crystal structure of the catalysts. In Fig. 3a, the XRD diffraction peaks of simulated PCN-222 are consistent with those of prepared PCN-222, PCN-222-Co and PCN-222-Fe, indicating that PCN-222, PCN-222-Co and PCN-222-Fe have been successfully prepared with the crystal structure of simulated PCN-222 (Fig. S4, ESI<sup>†</sup>). For  $\text{TiOF}_2$ , obvious peaks can be observed at  $23^\circ$ ,  $33^\circ$  and  $48^\circ$  in Fig. 3a, corresponding to the diffraction peaks of (100), (110) and (200) of JCPDS 08-0060, which proves the successful synthesis of  $\text{TiOF}_2$ . Similarly, for PCN-222, obvious peaks can be observed at  $4.9^\circ$ ,  $7.1^\circ$  and  $9.9^\circ$ , corresponding to the diffraction peaks of (200), (201) and (221). For the composite  $\text{TiOF}_2$ @PCN-222-Fe, the diffraction peaks at  $4.9^\circ$ ,  $7.1^\circ$  and  $9.9^\circ$  for the (200), (201) and (221) facets of PCN-222-Fe and the diffraction peaks at  $23^\circ$ ,  $33^\circ$  and  $48^\circ$  for the (100), (110) and (200) facets of  $\text{TiOF}_2$  can be observed simultaneously, which proves the successful combination of PCN-222-Fe and  $\text{TiOF}_2$  in the composite. As shown in Fig. S4 (ESI<sup>†</sup>), new diffraction peaks for cystine (Cys) were observed at  $18^\circ$  and  $28^\circ$  in  $\text{TiOF}_2$ @PCN-222-Fe and Cys-PCN-222, which come from loss of  $\text{H}_2$  of two

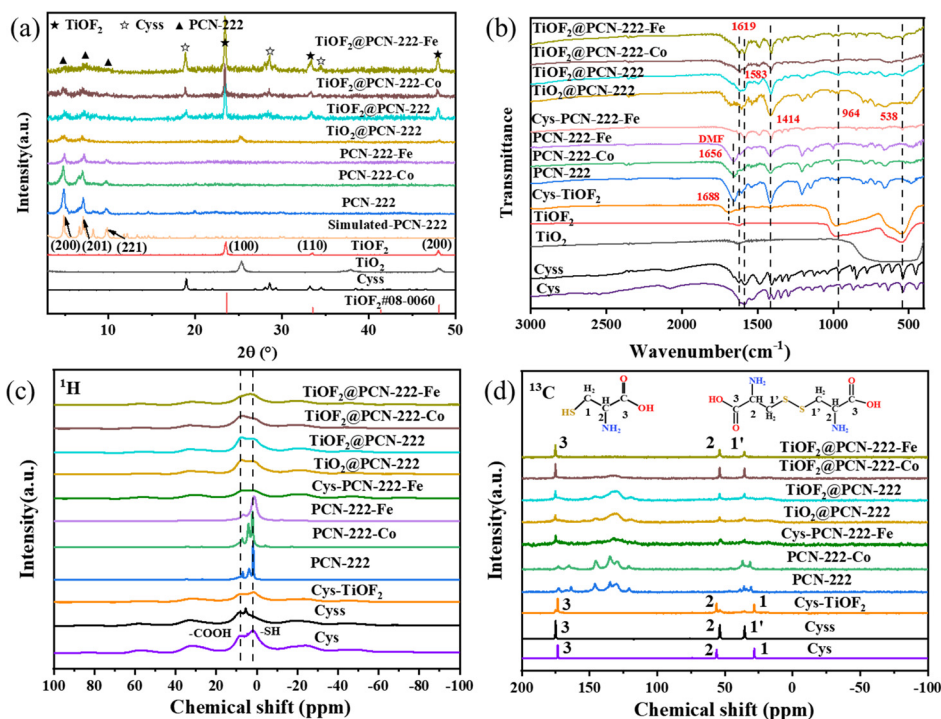


Fig. 3 (a) PXRD patterns and (b) FT-IR and (c)  $^1\text{H}$  and (d)  $^{13}\text{C}$ -NMR spectra of L-cysteine, cystine,  $\text{TiOF}_2$ , Cys- $\text{TiOF}_2$  and PCN-222 series complexes.

L-cysteine (Cys) molecules to form the S–S bond of cyss, while there is no peak for L-cysteine or cystine observed for Cys-TiOF<sub>2</sub>. These results suggest the different coordination abilities of the –SH group and the –COOH group of L-cysteine in the respective PCN-222 and TiOF<sub>2</sub> nanoparticles, implying that the –COOH group in cys coordinated with Ti<sup>4+</sup> in TiOF<sub>2</sub> and cannot form the S–S bond to produce cyss. Inductively coupled plasma optical emission spectroscopy (ICP-OES) was used to accurately obtain the amount of each element in the composites shown in Table S2 (ESI†). The presence of the Co, Fe, Ti, and F elements indicates that PCN-222 and TiOF<sub>2</sub> have been successfully combined. To investigate the specific bonding of the composites, FT-IR spectroscopy and <sup>1</sup>H and <sup>13</sup>C solid state NMR were performed, as shown in Fig. 3. In Fig. 3b for the pure TiOF<sub>2</sub> sample, the peak at 538 cm<sup>-1</sup> is assigned to the  $\nu_{\text{Ti-F}}$  modes associated with TiO<sub>2</sub>F<sub>4</sub> octahedra in TiOF<sub>2</sub>, the band at 964 cm<sup>-1</sup> is attributed to the terminal oxygen  $\nu_{\text{Ti=O}}$  mode in TiOF<sub>2</sub>, and the peak at 1630 cm<sup>-1</sup> is associated with the surface hydroxyl oxygen group (–OH). The peak of the sulfhydryl (–SH) group in pure L-cysteine is located at 2555 cm<sup>-1</sup>; no peak at 2555 cm<sup>-1</sup> was observed for pure cystine due to the formation of the S–S bond. In all L-cysteine-treated samples, there is also no peak at 2555 cm<sup>-1</sup>. It is suggested that the absorption peak of the SH group itself is very weak and is too low to be detected by FT-IR in the L-cysteine-treated samples. For Cys-TiOF<sub>2</sub> (calcining pure TiOF<sub>2</sub> with L-cysteine at 200 °C), the peaks at 1688 and 1414 cm<sup>-1</sup> belong to the asymmetric ( $\nu_a$ ) and symmetric stretching vibrations ( $\nu_s$ ) of the –COO<sup>-</sup> group in the monodentate coordinated L-cysteine with Ti<sup>4+</sup>. It is reported that the value of  $\Delta = \nu_a - \nu_s$  for the monodentate coordinated –COO<sup>-</sup> group is higher than that for the bidentate coordinated –COO<sup>-</sup> group.<sup>36</sup>

For Cys-PCN-222-Fe samples (calcining PCN-222-Fe with L-cysteine at 200 °C), the peak at 1619 cm<sup>-1</sup> attributed to the primary amine (–NH<sub>2</sub>) group in pure L-cysteine or cystine remained unchanged, implying that the –NH<sub>2</sub> group is not coordinated, and the peaks at 1583 cm<sup>-1</sup> and 1414 cm<sup>-1</sup> correspond to the asymmetric and symmetric stretching vibrations of the bidentate coordinated –COO<sup>-</sup> group in PCN-222-Fe, respectively. These results indicated that –the COOH group in L-cysteine coordinated with TiOF<sub>2</sub>, while the –SH group in L-cysteine coordinated with Fe<sup>3+</sup> in PCN-222-Fe and the primary amine (–NH<sub>2</sub>) group in L-cysteine is not coordinated. For pure PCN-222/Co/Fe, the peak at 1656 cm<sup>-1</sup> is attributed to C=O in the DMF solvent absorbed in the pores of PCN-222/Co/Fe, which is confirmed by <sup>1</sup>H-NMR results in Fig. 3c. This peak disappeared for Cys-PCN-222-Fe and TiOF<sub>2</sub>@PCN-222/Co/Fe composites. However, the peaks at 1583 cm<sup>-1</sup> and 1414 cm<sup>-1</sup> corresponding to the asymmetric and symmetric stretching vibrations of the bidentate coordinated –COO<sup>-</sup> group in PCN-222/Co/Fe remained unchanged in Cys-PCN-222-Fe and TiOF<sub>2</sub>@PCN-222/Co/Fe composites, indicating that the structure of PCN-222/Co/Fe remained unchanged in Cys-PCN-222-Fe and TiOF<sub>2</sub>@PCN-222/Co/Fe composites. The peak at 1500 cm<sup>-1</sup> assigned to the N–H plane bending vibration in cystine is also observed for the composites. At the same time, TiOF<sub>2</sub> peaks at 964 cm<sup>-1</sup> and 538 cm<sup>-1</sup> appeared for the composite samples,

indicating that the TiOF<sub>2</sub>@PCN-222-Fe heterojunction was successfully prepared. It is very meaningful that in the <sup>1</sup>H-NMR spectra (Fig. 3c) of pure L-cysteine, two obvious peaks at 1.5 and 8 ppm are observed, which are assigned to protons in the –SH group and –COOH group respectively. For pure cystine, due to the loss of H<sub>2</sub> and the formation of the S–S bond, the peak at 1.5 ppm for the –SH group disappeared. The coordination information of L-cysteine in the TiOF<sub>2</sub>@PCN-222-Fe composite can thus be easily judged according to the proportion of the two peaks for –SH and –COOH groups. For L-cysteine-treated Cys-TiOF<sub>2</sub>, the peak area for the –SH group is higher than that for the –COOH group, indicating that the –SH group did not coordinate with Ti<sup>4+</sup>, but the –COOH group coordinated with Ti<sup>4+</sup> by substituting the surface hydroxyl (OH<sup>-</sup>) of TiOF<sub>2</sub> with –COO<sup>-</sup>. For L-cysteine-treated Cys-PCN-222-Fe, in <sup>1</sup>H-NMR spectra the peak area for the –SH group is lower than that for the –COOH group, indicating that the –COOH group did not coordinate with Fe<sup>3+</sup> but the –SH group axially coordinated with Fe<sup>3+</sup> by substituting the Cl<sup>-</sup> ion in PCN-222-Fe with –S<sup>-</sup>. The sharp peaks observed at 2, 4 and 7 ppm for pure PCN-222/Co/Fe are attributed to DMF solvent absorbed in the pores. These findings can also be confirmed by <sup>13</sup>C-NMR spectra shown in Fig. 3d. The peaks at 28, 56, 174 ppm for pure L-cysteine are attributed to C1 connected with the –SH group, C2 connected with the –NH<sub>2</sub> group, and C3 in the –COOH group respectively. For L-cysteine-treated Cys-TiOF<sub>2</sub>, the chemical shifts remained almost unchanged as L-cysteine and less cystine are formed, implying that L-cysteine combined with TiOF<sub>2</sub> through the –COOH group without cystine forming. For L-cysteine-treated Cys-PCN-222-Fe, cystine is found to be formed with the chemical shift at 36, 54, and 175 ppm, indicating that the –COOH group is not coordinated and part of the –SH group is coordinated with Fe<sup>3+</sup>, and thus the residual unbound L-cysteine lost H<sub>2</sub> to form cystine. In <sup>13</sup>C spectra, the peaks around 120–140 ppm are assigned to C in the benzene ring and the peak at 175 ppm is assigned to carboxyl C. The peaks of the benzene ring in the TCPP ligand cannot be observed for TiOF<sub>2</sub>@PCN-222-Fe due to the strong magnetism of Fe as observed by EPR results shown in Fig. S8 (ESI†). The <sup>1</sup>H and <sup>13</sup>C NMR spectra demonstrated that in TiOF<sub>2</sub>@PCN-222-Fe composites the –SH group coordinated with Fe<sup>3+</sup> and –the COOH group coordinated with Ti<sup>4+</sup>, and thus, TiOF<sub>2</sub> and PCN-222-Fe are bonded together through L-cysteine.

To further demonstrate the agglomeration of TiOF<sub>2</sub> with PCN-222/Co/Fe through L-cysteine, several characterization techniques were used to study the structure of TiOF<sub>2</sub>@PCN-222/Co/Fe composites. Fig. 4 and Fig. S5 (ESI†) show the UV-vis diffuse reflectance spectra (UV-vis-DRS) of the samples. For the feature absorption of the TCPP ligand in PCN-222, electron transition from the high-occupied molecular orbital  $\alpha_{1\mu}(\pi)$  to the lowest-unoccupied orbital  $e_g(\pi^*)$  produces the strong absorption of the Soret band at around 420 nm and the  $\alpha_{2\mu}(\pi)$ – $e_g(\pi)$  electron transition is in the 500–670 nm range, which produces four weak absorption Q bands. According to Fig. 4, for the PCN-222 sample the Soret band appears at 443 nm and four weak adsorption Q bands are located at 515, 550, 590 and 648 nm, respectively. On the other hand, PCN-222-Co and PCN-222-Fe show a decrease

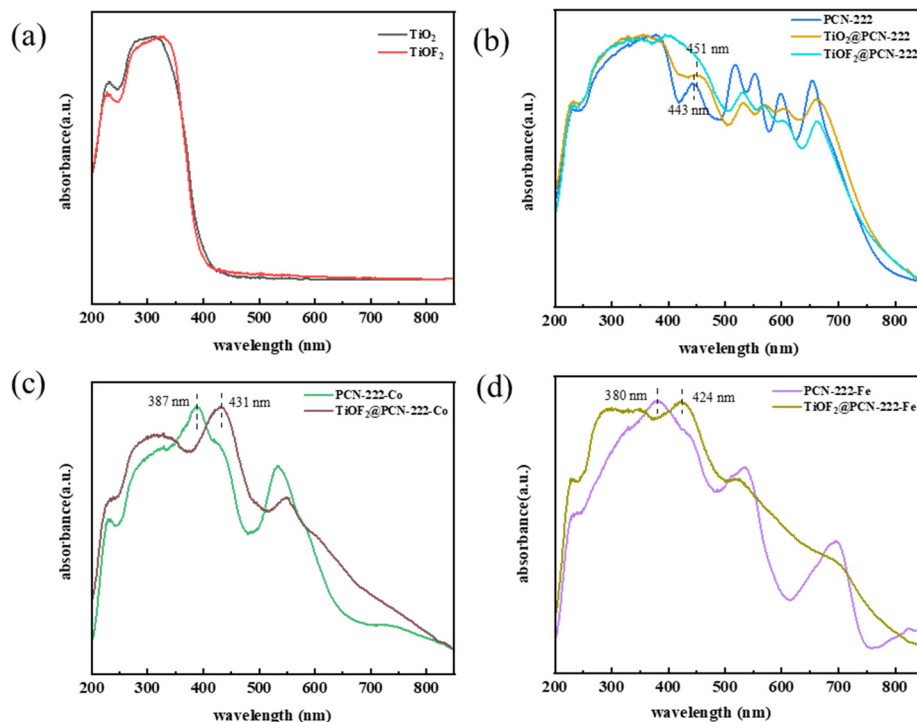


Fig. 4 UV-vis DRS spectra of (a)  $\text{TiO}_2$  and  $\text{TiOF}_2$ , (b) PCN-222,  $\text{TiO}_2$ @PCN-222 and  $\text{TiOF}_2$ @PCN-222, (c) PCN-222-Co and  $\text{TiOF}_2$ @PCN-222-Co, and (d) PCN-222-Fe and  $\text{TiOF}_2$ @PCN-222-Fe.

in the number of absorption peaks and the weakening of the peak intensity of the Q band as shown in Fig. 4b and c, which is the spectral feature of the corresponding porphyrin complexes TCPP-Co and TCPP-Fe.<sup>37</sup> After the agglomeration of PCN-222/-Co/-Fe and  $\text{TiOF}_2$ , due to the axial coordination of *L*-cysteine with the TCPP/-Co/-Fe ligand through the -SH group, the red-shifts of the Soret band for the  $\text{TiOF}_2$ @PCN-222/-Co/-Fe composites are observed at 443  $\rightarrow$  451, 387  $\rightarrow$  431, and 380  $\rightarrow$  424 nm, respectively. This can be explained<sup>37</sup> by the fact that the lone-pair electron on the S atom of *L*-cysteine is an electron donor and can be conjugated with the  $\pi$  electron of the porphyrin ring, which increases the electron density of the porphyrin ring and the energy levels of  $\alpha_{1\mu}(\pi)$  and  $\alpha_{2\mu}(\pi)$  orbitals, thus narrowing the energy level distance between the two  $\alpha_{1\mu}(\pi)$  and  $\alpha_{2\mu}(\pi)$  orbitals and the  $e_g(\pi)$  orbital, so the Soret bands of the UV-vis DRS spectra of  $\text{TiOF}_2$ @PCN-222/-Co/-Fe are red-shifted as reported in the literature.<sup>38,39</sup> From UV-vis-DRS spectra shown in Fig. S5 (ESI<sup>†</sup>), the results of *L*-cysteine axial coordination with TCPP/-Co/-Fe through the -SH group are further confirmed. Cys-PCN-222 also shows red shifts in the Soret bands from 400 nm to 450 nm; it is suggested that the four pyrrole N atoms in TCPP porphyrin can be easily protonated by the -SH group of *L*-cysteine. On the other hand, Cys- $\text{TiOF}_2$  shows obvious absorbance of visible light at 400–700 nm compared with pure  $\text{TiOF}_2$ , which indicates that *L*-cysteine coordination with  $\text{TiOF}_2$  through the -COOH group results in the increased absorption of visible light as we reported for  $\text{NH}_2$ -MIL-125.<sup>40</sup>

According to the shifts in binding energy (BE) for elements such as Ti 2p, F 1s, Zr 3d, S 2p, Fe 2p, and Cl 2p (Fig. 5 and

Fig. S6, ESI<sup>†</sup>), XPS results can provide detailed information about the agglomeration of  $\text{TiOF}_2$  and PCN-222-Fe through the -COOH and -SH groups of *L*-cysteine, respectively. In Fig. 5a, the BE of Ti 2p for  $\text{TiOF}_2$  (458.8 eV) is higher than that for  $\text{TiO}_2$  (458.5 eV), indicating that F element has an electron-withdrawing effect on Ti element. On the other hand, for Cys- $\text{TiOF}_2$  and  $\text{TiOF}_2$ @PCN-222-Fe, a new peak at a much higher BE of Ti 2p (459.8 eV) assigned to COO-Ti is observed, indicating that -COO<sup>-</sup> in *L*-cysteine coordinated with  $\text{Ti}^{4+}$  can also have an electron-withdrawing effect on Ti element. Similarly, it can be seen from Fig. 5d that the BEs of S 2p for Cys-PCN-222-Fe and  $\text{TiOF}_2$ @PCN-222-Fe wholly shift to higher values than those of pure cystine or *L*-cysteine, and a new peak at a much higher BE of S 2p (164.9 eV) assigned to S-Fe is observed compared with that for pure cystine or *L*-cysteine (162.8 eV), indicating the axial coordination -of S<sup>-</sup> with Fe<sup>3+</sup> in the composites. The BE of F 1s as shown in Fig. 5b remains nearly unchanged. In Fig. 5c, the BE of Zr 3d for PCN-222-Fe is higher than that for pure  $\text{ZrO}_2$ , also indicating that the -COO<sup>-</sup> group in the TCPP-Fe ligand has an electron-withdrawing effect on Zr element. The BEs of Zr 3d for Cys-PCN-222-Fe and  $\text{TiOF}_2$ @PCN-222-Fe are much lower than that for pure PCN-222-Fe, suggesting that  $\text{Zr}^{4+}$  in Cys-PCN-222-Fe and  $\text{TiOF}_2$ @PCN-222-Fe gain electrons due to the increasing amount of oxygen vacancies as confirmed by subsequent EPR results in Fig. S8 (ESI<sup>†</sup>). Similar results are observed for Fe 2p; as shown in Fig. 5e, the BE of Fe 2p for Cys-PCN-222-Fe and  $\text{TiOF}_2$ @PCN-222-Fe is much lower than that for pure PCN-222-Fe, also suggesting the electron-donating effect of S<sup>-</sup> on Fe<sup>3+</sup>. Moreover, as shown in Fig. 5f, Cl 2p is observed due to Cl<sup>-</sup> in

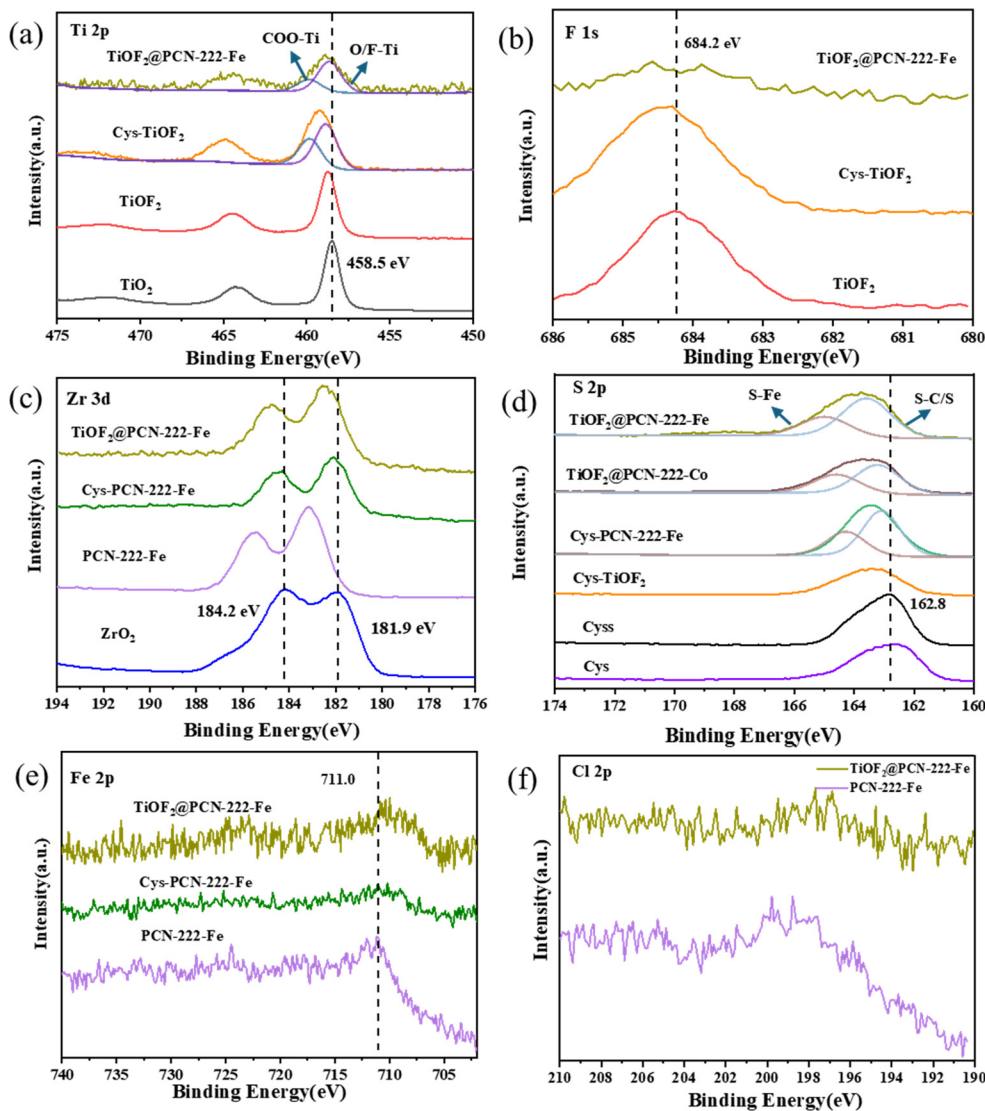


Fig. 5 XPS results of  $\text{TiO}_2$ ,  $\text{TiOF}_2$  and PCN-222 series complexes. (a) Ti 2p, (b) F 1s, (c) Zr 3d, (d) S 2p, (e) Fe 2p, and (f) Cl 2p.

PCN-222-Fe with a formula of  $\text{C}_{96}\text{H}_{64}\text{Cl}_2\text{Fe}_2\text{N}_8\text{O}_{32}\text{Zr}_6$ . After the combination of  $\text{TiOF}_2$  and PCN-222-Fe with *L*-cysteine, the intensity of Cl 2p decreased obviously, indicating that the  $-\text{S}^-$  substituted  $\text{Cl}^-$  and  $-\text{S}^-$  groups axially coordinated with  $\text{Fe}^{3+}$ . As shown in Fig. S6 (ESI<sup>†</sup>), the BE of Co 2p also shifts to the lower side after the combination of  $\text{TiOF}_2$  and PCN-222-Co with *L*-cysteine, also indicating the electron-donating effect of the S atom on  $\text{Co}^{2+}$ . The coordination ability of the  $-\text{NH}_2$  group is lower than those of  $-\text{COOH}$  and  $-\text{SH}$  groups. The BEs (400.5 eV) of N 1s for Cys-PCN-222-Fe and  $\text{TiOF}_2$ @PCN-222-Fe are not different from those of Cys and Cyss, indicating that the amino group in *L*-cysteine does not participate in the coordination. The BE (399.2 eV) of N 1s for cys- $\text{TiOF}_2$  became lower due to the deprotonation of the protonated  $-\text{NH}_2$  group with the formation of  $-\text{COO-Ti}$ , which shows the same BE (399.2 eV) as we reported for  $\text{NH}_2\text{-MIL-125}$ .<sup>40</sup> On the other hand, the  $-\text{COOH}$  group and  $-\text{SH}$  group are involved in the coordination of  $\text{Ti}^{4+}$  and  $\text{Fe}^{3+}$  respectively as shown by the BE results of Ti 2p and Fe

2p. These observations further support our proposed mechanism of the agglomeration of  $\text{TiOF}_2$  with PCN-222-Fe through the  $-\text{COOH}$  and  $-\text{SH}$  groups of self-assembled *L*-cysteine.

To explore the inherent structure and coordination environment at the atomic level of  $\text{TiOF}_2$ @PCN-222-Fe, the X-ray absorption fine structure (XAFS) spectroscopy analysis of the Fe K-edge and Ti K-edge was carried out. The K-edge XANES of  $\text{TiOF}_2$ @PCN-222-Fe (Fig. 6a and b) showed that Fe element exhibited +3 valence as  $\text{Fe}_2\text{O}_3$  and Ti element exhibited +4 valence as  $\text{TiO}_2$ . The peak intensity of the white line decreased for the Fe K-edge of  $\text{TiOF}_2$ @PCN-222-Fe compared with that of pure PCN-222-Fe, and the peak intensity of the white line decreased for the Ti K-edge of  $\text{TiOF}_2$ @PCN-222-Fe compared with that of pure  $\text{TiOF}_2$ . This result reveals that the coordination environments for  $\text{Fe}^{3+}$  and  $\text{Ti}^{4+}$  in  $\text{TiOF}_2$ @PCN-222-Fe are different from those for  $\text{Fe}^{3+}$  and  $\text{Ti}^{4+}$  in pure PCN-222-Fe and pure  $\text{TiOF}_2$ , providing important evidence for the coordination of *L*-cysteine with  $\text{Fe}^{3+}$  through the  $-\text{SH}$  group and with  $\text{Ti}^{4+}$

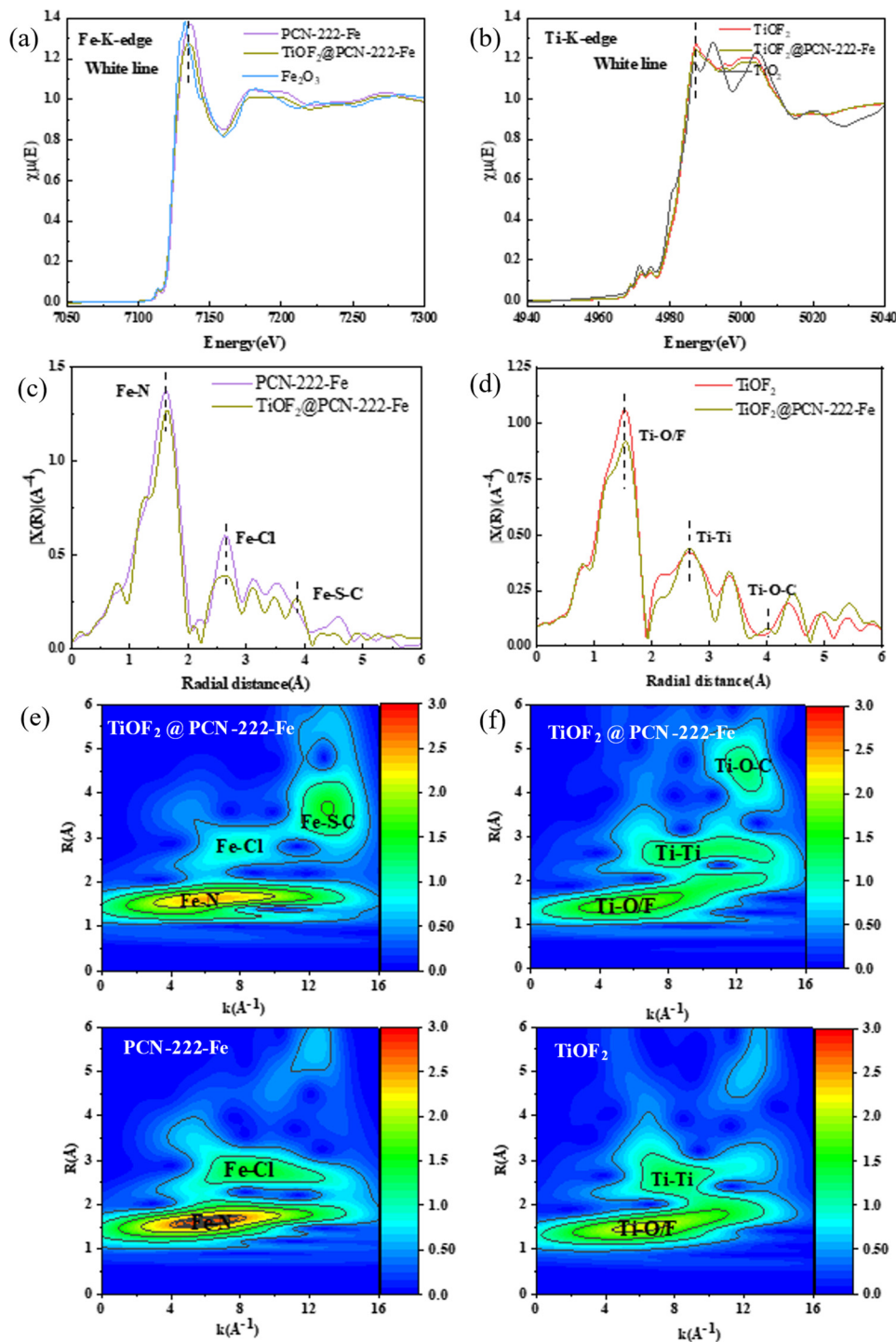


Fig. 6 (a) Enlarged X-ray absorption near edge structure (XANES) spectra of the Fe K-edge, (b) XANES spectra of the Ti K-edge, (c) extended X-ray absorption fine structure (EXAFS) spectra of the Fe K-edge, (d) EXAFS spectra of the Ti K-edge, (e) Fe K-edge whole contour plots of the wavelet transforms (WTs) of  $\text{TiOF}_2@PCN-222\text{-Fe}$  and  $PCN-222\text{-Fe}$ , and (f) Ti K-edge whole contour plots of the wavelet transforms (WTs) of  $\text{TiOF}_2@PCN-222\text{-Fe}$  and  $\text{TiOF}_2$ .

through the  $-\text{COOH}$  group in  $\text{TiOF}_2@PCN-222\text{-Fe}$ . The Fourier transform (FT) extended X-ray absorption fine structure (EXAFS) curves of the Fe K-edge are shown in Fig. 6c; two interatomic distances of 1.7 and 2.7 Å in the first shell are assigned to Fe-N and Fe-Cl bonds in  $PCN-222\text{-Fe}$ , and a dominant new peak at

3.8 Å in the second shell was observed for  $\text{TiOF}_2@PCN-222\text{-Fe}$  compared with that for pure  $PCN-222\text{-Fe}$ , which can be attributed to Fe-S-C bonding formed by the coordination of L-cysteine with  $\text{Fe}^{3+}$  through the  $-\text{SH}$  group. The EXAFS spectra of the Ti K-edge are shown in Fig. 6d; two interatomic distances of 1.6 and 2.7 Å in

the first shell are assigned to Ti–O/F and Ti–Ti bonds in TiOF<sub>2</sub>, and a dominant new peak at 4.0 Å in the second shell was observed for TiOF<sub>2</sub>@PCN-222-Fe compared with that for pure TiOF<sub>2</sub>, which can be attributed to Ti–O–C bonding formed by the coordination of L-cysteine with Ti<sup>4+</sup> through the –COOH group. The wavelet transforms (WTs) of Fe and Ti K-edge whole contour plots are shown in Fig. 6e and f. New bonding of Fe–S–C and Ti–O–C is also observed in TiOF<sub>2</sub>@PCN-222-Fe compared with that in pure PCN-222-Fe and TiOF<sub>2</sub>, further indicating the coordination of L-cysteine with Fe<sup>3+</sup> through the –SH group and with Ti<sup>4+</sup> through the –COOH group.

Potentiometric acid–base titration was used to quantitatively study the amount of –OH hydroxyl group in the samples. The potentiometric acid–base titration curve and the corresponding first derivative curve are shown in Fig. S7 and Table S3 (ESI<sup>†</sup>). All samples show pK<sub>a</sub> values at about ~3.30, indicating the existence of the –OH group including surface Ti–OH in TiOF<sub>2</sub>, Zr–OH in PCN-222/-Co/-Fe and –COOH in L-cysteine/cystine. PCN-222-Fe has one obvious titration mutation point (pK<sub>a</sub> ~ 3.30), which is assigned to the bridging three-coordinated μ<sub>3</sub>-OH in the Zr<sub>6</sub>O<sub>8</sub>(μ<sub>3</sub>-OH)<sub>8</sub> cluster. In Table S3 (ESI<sup>†</sup>), all samples use the same mass of 25 mg; the mass ratio of Cys/PCN-222/TiOF<sub>2</sub> in TiOF<sub>2</sub>@PCN-222/-Co/-Fe samples is 10 : 8 : 2. The moles of NaOH (*n*<sub>NaOH</sub>) used for TiOF<sub>2</sub>@PCN-222/-Co/-Fe (~8.80 × 10<sup>-5</sup> mol) obviously increased compared with that for TiO<sub>2</sub>@PCN-222 (~6.28 × 10<sup>-5</sup> mol), suggesting the increasing amount of the –OH group in TiOF<sub>2</sub>@PCN-222/-Co/-Fe. This result can be explained by the subsequent EPR results in Fig. S8 (ESI<sup>†</sup>) that increasing amounts of oxygen vacancies are observed in TiOF<sub>2</sub>@PCN-222/-Co/-Fe. In the Zr<sub>6</sub>O<sub>8</sub>(μ<sub>3</sub>-OH)<sub>8</sub> cluster of PCN-222/-Co/-Fe the adjacent Zr<sup>4+</sup> node can form the hydroxyl Zr–OH group when one Zr<sup>4+</sup> node loses a carboxylic acid (–COOH) ligand to form an oxygen vacancy, and thus the amount of *n*<sub>NaOH</sub> is enhanced. This makes the transmission pathway of the protons through the hydroxyl group (–OH) in the heterojunction photocatalysts more smooth and conducive to H<sub>2</sub>O oxidation and CO<sub>2</sub> reduction.

To illustrate the existence of unpaired electrons in the composite catalysts, electron paramagnetic resonance spectroscopy (EPR) was used. The results are shown in Fig. S8 (ESI<sup>†</sup>). It can be seen that pure TiOF<sub>2</sub> and pure PCN-222-Fe have very low signals at *g* = 2.004 attributed to unpaired electrons. However, the composite samples all show an obviously increased signal at *g* = 2.004, which is due to the increasing amount of oxygen vacancies with electrons trapped inside. We previously reported that UiO-66 with the Zr<sub>6</sub>O<sub>4</sub>(OH)<sub>4</sub>(CO<sub>2</sub>)<sub>12</sub> formula can also generate oxygen vacancies in Zr<sup>4+</sup> nodes with electrons trapped inside.<sup>38</sup> Although the sulfhydryl radical is also observed in pure L-cysteine and cystine as shown in Fig. S8b (ESI<sup>†</sup>), the signal at *g* = 2.004 is very weak. L-cysteine loses an electron of the sulfhydryl group and forms a sulfhydryl radical. The radical is unstable and easily dimerizes to form cystine. The intensity of the EPR signal at *g* = 2.004 for TiOF<sub>2</sub>@PCN-222-Fe and TiOF<sub>2</sub>@PCN-222-Co is lower than that for TiOF<sub>2</sub>@PCN-222, implying that L-cysteine coordinating with PCN-222-Fe/Co decreases the amount of oxygen vacancies.

## 2.2. Performance study of photocatalytic reduction of CO<sub>2</sub>

Photocatalytic reduction of CO<sub>2</sub> (CO<sub>2</sub>RR) was performed on TiOF<sub>2</sub>@PCN-222/-Co/-Fe composites under a 300 W Xe lamp with a 420 nm filter to obtain visible light. The CO<sub>2</sub>RR activities for the production of carbon monoxide CO on each catalyst are shown in Fig. 7a. Compared with the TiO<sub>2</sub>-based TiO<sub>2</sub>@PCN-222-Fe composite, the TiOF<sub>2</sub>-based TiOF<sub>2</sub>@PCN-222-Fe composite exhibits higher photoreduction properties. Calculated from the standard curve (Fig. S9, ESI<sup>†</sup>), the CO production by TiOF<sub>2</sub>@PCN-222-Fe was the highest (6.72 μmol g<sup>-1</sup>), which was nearly 10 times that of TiO<sub>2</sub>. The order of the CO<sub>2</sub>RR activity of the composites is TiOF<sub>2</sub>@PCN-222-Fe > TiOF<sub>2</sub>@PCN-222-Co > TiOF<sub>2</sub>@PCN-222 > TiO<sub>2</sub>@PCN-222-Fe > TiO<sub>2</sub>@PCN-222. This result indicates a superior synergistic effect between TiOF<sub>2</sub> and PCN-222-Fe through L-cysteine. To investigate the stability of the TiOF<sub>2</sub>@PCN-222-Fe catalyst, three repeated photocatalytic experiments were performed. The samples were recovered and dried before the next use. After three cycles, a CO yield of 4.82 μmol g<sup>-1</sup> can be obtained as shown in Fig. 7b, which is 71% of the first test. After the reproducible experimental tests, the used catalyst was tested by FT-IR, XRD, and XPS (Fig. S10 and S11, ESI<sup>†</sup>). Little changes in FT-IR and XRD spectra are found, indicating that the catalyst structure remained unchanged before and after the CO<sub>2</sub>RR reaction. Comparison of the XPS spectra of the TiOF<sub>2</sub>@PCN-222-Fe catalyst before and after the CO<sub>2</sub>RR reaction shows that a little change in BEs was found for Ti, O, Fe, and N elements, while it is worth noting that a shoulder peak at lower BE (182 eV) for Zr 3d is found for the used catalyst, indicating that the photogenerated holes in PCN-222-Fe oxidize H<sub>2</sub>O to O<sub>2</sub>, and the photogenerated electrons in PCN-222-Fe are partially gained by Zr<sup>4+</sup>, resulting in lower BE for Zr 3d. To determine the source of the CO product, a <sup>13</sup>CO<sub>2</sub> isotope labeling experiment was performed on TiOF<sub>2</sub>@PCN-222-Fe, in which the products were detected by GC-MS. As shown in Fig. 7e and f, after <sup>13</sup>CO<sub>2</sub> was photocatalyzed for 4 h in a quartz reactor, the product was obtained as a mixed gas. The scan mode was adopted to detect the presence of <sup>13</sup>CO (*m/z* = 29) in the products. In the total ion chromatogram (TIC), the peak at 5.22 min corresponding to <sup>13</sup>CO is observed. Its mass spectrum is mainly composed of three signals, a signal peak at *m/z* = 29 (<sup>13</sup>CO) and two other fragments at *m/z* = 13 (<sup>13</sup>C) and *m/z* = 16 (<sup>16</sup>O), confirming that the CO product was derived from CO<sub>2</sub> reduction. In addition, the electrocatalytic oxygen evolution reaction (OER) performances of the catalysts were characterized to clarify the active site for the half-reaction of photocatalytic oxygen production. As can be seen from Fig. 7c, when the current density reaches 0.2 mA cm<sup>-2</sup>, the voltage required for TiOF<sub>2</sub>@PCN-222-Fe is 1.488 V, while the voltages required for pure TiOF<sub>2</sub> and pure PCN-222-Fe are 1.546 V and 1.595 V, respectively. At the same current density, TiOF<sub>2</sub>@PCN-222-Fe requires the lowest overpotential for the OER, indicating that it shows the best oxygen evolution performance. Moreover, the OER initial potential for TiOF<sub>2</sub>@PCN-222-Fe is the same as that for pure TiOF<sub>2</sub> and is much lower than that for pure PCN-222-Fe, while the OER polarization curve at high current density above 1.0 mA cm<sup>-2</sup> for TiOF<sub>2</sub>@PCN-222-Fe is the same as that for pure PCN-222-Fe and is much higher than that for pure TiOF<sub>2</sub>.

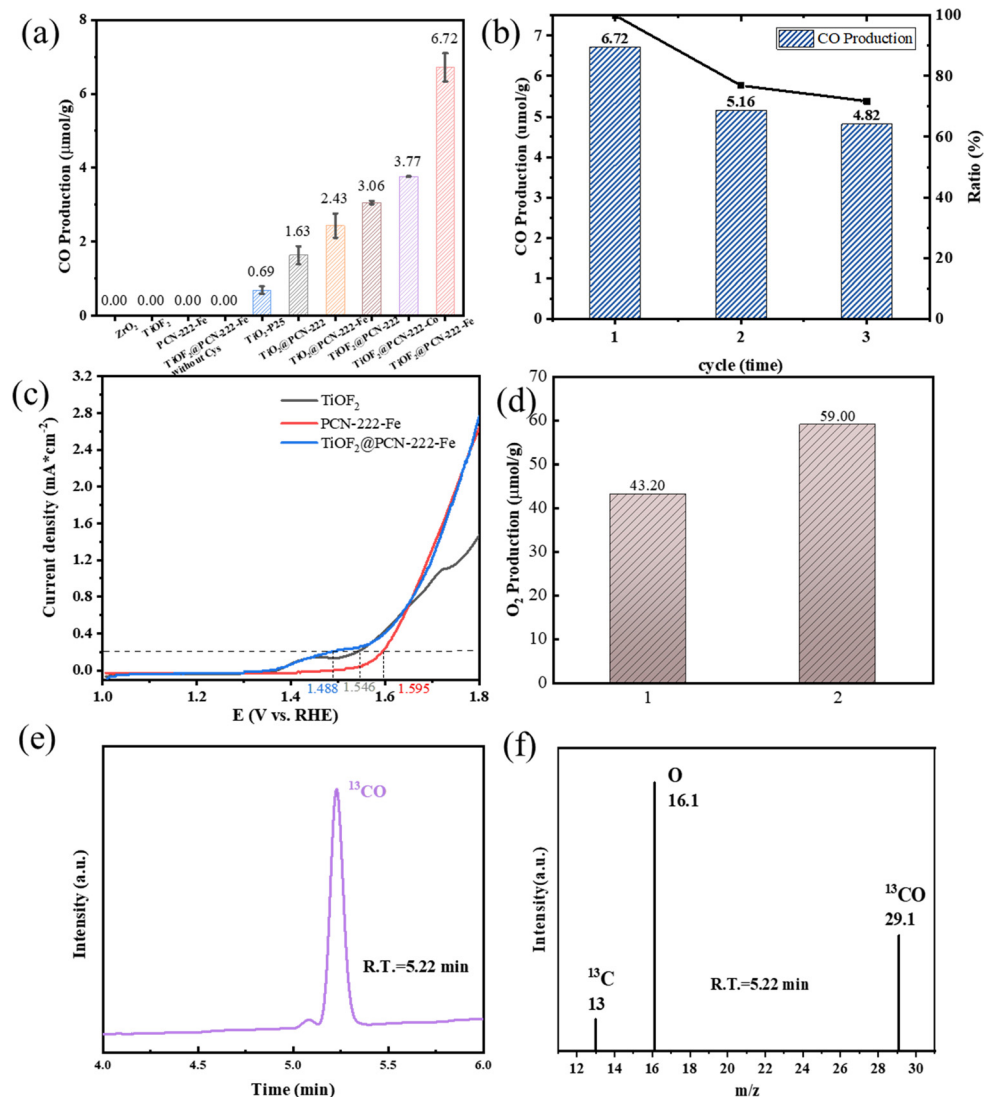


Fig. 7 (a) Comparison of the amount of CO produced over the photocatalyst. (b) The recycle experiment of TiO<sub>2</sub>@PCN-222-Fe. (c) OER performance test of TiO<sub>2</sub>, PCN-222-Fe and TiO<sub>2</sub>@PCN-222-Fe. (d) O<sub>2</sub> production in the OER of H<sub>2</sub>O photocatalysis using TiO<sub>2</sub>@PCN-222-Fe. (e) and (f) GC-MS spectra of <sup>13</sup>C-containing products over TiO<sub>2</sub>@PCN-222-Fe in the photocatalytic reduction of <sup>13</sup>CO<sub>2</sub>.

This result indicates that TiO<sub>2</sub>@PCN-222-Fe combined the advantages of the two raw materials and the OER activity of TiO<sub>2</sub>@PCN-222-Fe is mainly attributed to PCN-222-Fe rather than TiO<sub>2</sub>. Besides, in Fig. 7d, the photocatalytic activity for the OER of H<sub>2</sub>O using TiO<sub>2</sub>@PCN-222-Fe was investigated. The experiments are conducted two times and the result shows that the O<sub>2</sub> production is 43.2 and 59.0 μmol g<sup>-1</sup> after illumination, indicating that TiO<sub>2</sub>@PCN-222-Fe possesses good OER photocatalytic activity.

### 2.3. Photoelectrochemical performance evaluation

The optoelectronic performance tests were carried out on the catalysts to gain insight into the high visible light photocatalytic CO<sub>2</sub> reduction performance of TiO<sub>2</sub>@PCN-222-Fe composites. Fig. 8a–d shows the optoelectronic properties of the TiO<sub>2</sub>@PCN-222-Fe series catalysts, and the effect of carrier separation efficiency of the composites is studied. The photocurrent–time (*I*–*t*) curve (Fig. 8a) shows that the photocurrent

intensity of the TiO<sub>2</sub>@PCN-222-Fe composite catalyst is significantly enhanced compared to any one component alone, indicating the enhanced photo-generated carrier concentration under 1-cysteine. The electrochemical impedance diagram can effectively reflect the carrier transport resistance of the TiO<sub>2</sub>@PCN-222-Fe photocatalyst, and it can be seen from Fig. 8b that the radius of the TiO<sub>2</sub>@PCN-222-Fe composite is smaller than that of PCN-222-Fe and TiO<sub>2</sub>, indicating that the charge transfer resistance at the TiO<sub>2</sub>@PCN-222-Fe interface is smaller. From the cyclic voltammetry curves (Fig. 8c), it is found that all of the catalysts can redox Fe<sup>2+</sup>/Fe<sup>3+</sup>; TiO<sub>2</sub>@PCN-222-Fe shows the highest current density, and thus the redox ability of TiO<sub>2</sub>@PCN-222-Fe is stronger than those of PCN-222-Fe and TiO<sub>2</sub>. The Fermi level of the semiconductors can be estimated using the Mott–Schottky (MS) curve (Fig. 8d and Fig. S12, ESI<sup>†</sup>). The positive slope shows that PCN-222-Fe and TiO<sub>2</sub> are

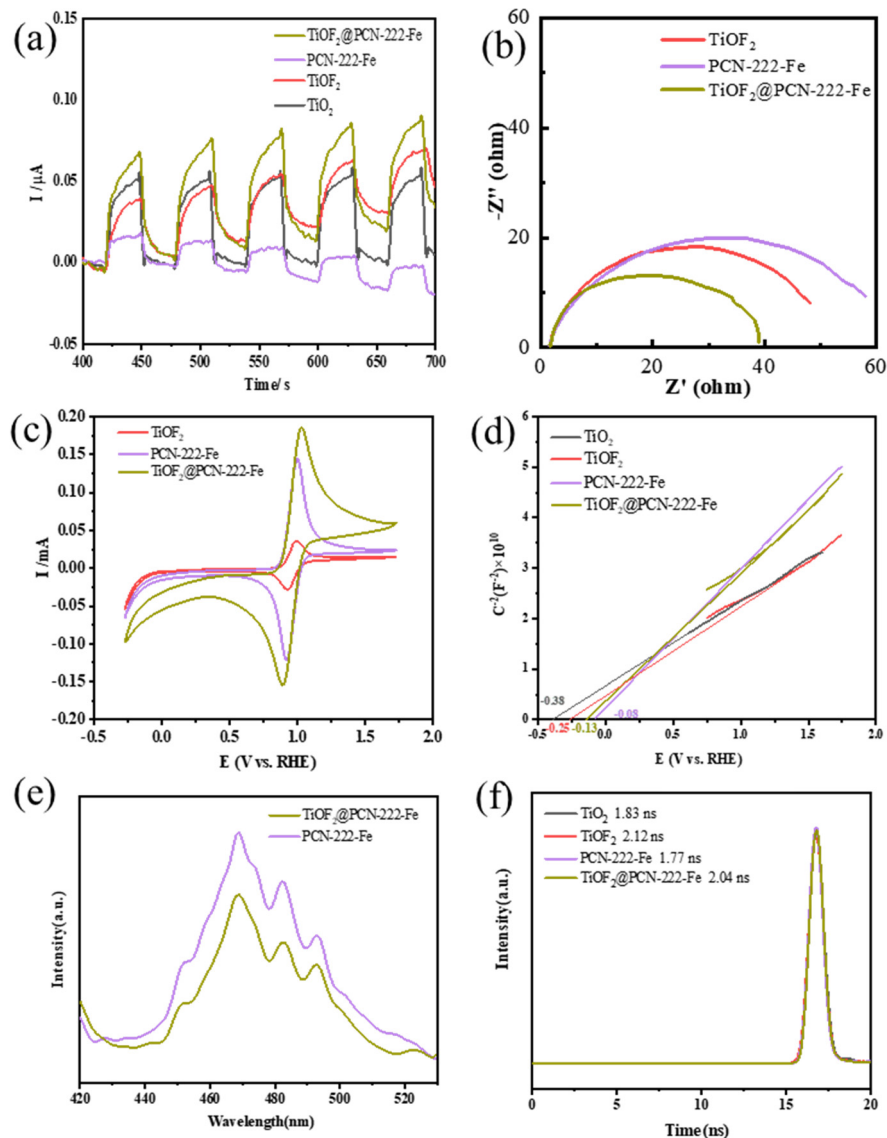


Fig. 8 (a) Photocurrent density curves. (b) Electrochemical impedance spectra. (c) Cyclic voltammograms of samples. (d) Mott–Schottky plots of samples in a 0.5 M aqueous solution of  $\text{Na}_2\text{SO}_4$ . (e) Photoluminescence spectra of samples. (f) Transient fluorescence spectra of  $\text{TiO}_2$ ,  $\text{TiOF}_2$ , PCN-222-Fe and  $\text{TiOF}_2@PCN-222\text{-Fe}$ .

both n-type semiconductors. The intercept of the x axis of the MS curve is equal to the flat band potential, which represents the Fermi level of the semiconductor. Thus the Fermi levels of pure  $\text{TiO}_2$ ,  $\text{TiOF}_2$ , PCN-222-Fe, and  $\text{TiOF}_2@PCN-222\text{-Fe}$  are estimated to be  $-0.38$ ,  $-0.25$ ,  $-0.08$ , and  $-0.13$  V vs. RHE, where the Fermi level of  $\text{TiOF}_2@PCN-222\text{-Fe}$  is between that of  $\text{TiOF}_2$  and PCN-222-Fe. Moreover, the Fermi level of  $\text{TiOF}_2$  is lower than that of  $\text{TiO}_2$ , implying that the electron-withdrawing effect of fluorine in  $\text{TiOF}_2$  lowered the Fermi level of  $\text{TiOF}_2$ . Huang *et al.*<sup>41,42</sup> constructed a hollow nanotube  $\text{Fe}_2\text{O}_3/\text{MoO}_3$  Z-scheme heterojunction. The Fermi levels of  $\text{Fe}_2\text{O}_3$  and  $\text{Fe}_2\text{O}_3/\text{MoO}_3$  were  $-4.08$  and  $-4.26$  eV (vs. vacuum), respectively. Due to the different Fermi levels after contact, the electrons entered  $\text{MoO}_3$  from the  $\text{Fe}_2\text{O}_3$  component and formed an internally connected electric field at the interface until the Fermi level

reached the same, during which the energy bands of both semiconductors were bent, and thus a Z-Scheme charge transport path was deduced.

Similarly, due to the different Fermi levels of  $\text{TiOF}_2$  and PCN-222-Fe, there is an energy difference between the two, which inevitably results in electron transfer to form a heterojunction. Ultraviolet photoelectron spectroscopy (UPS) measurements were performed to further investigate the Fermi levels calculated from the work functions of  $\text{TiOF}_2$ , PCN-222-Fe and  $\text{TiOF}_2@PCN-222\text{-Fe}$  as shown in Fig. S13 (ESI<sup>†</sup>). The work function ( $\Phi$ ), defined as the energy difference between the Fermi level and the vacuum level, is calculated to be 3.15, 3.89 and 3.6 eV for  $\text{TiOF}_2$ , PCN-222-Fe and  $\text{TiOF}_2@PCN-222\text{-Fe}$ , respectively. Thus, the Fermi level of  $\text{TiOF}_2$ , PCN-222-Fe and  $\text{TiOF}_2@PCN-222\text{-Fe}$  is calculated to be  $-3.15$ ,  $-3.89$  and

−3.6 eV (vs. vacuum level), respectively. The order of the Fermi level is consistent with the result obtained from the Mott–Schottky curve. That is to say, the Fermi level of TiO<sub>2</sub> (−3.15 eV) is higher than that of PCN-222-Fe (−3.89 eV); after the combination of TiO<sub>2</sub> and PCN-222-Fe, electrons will transfer from TiO<sub>2</sub> to PCN-222-Fe, also leading to higher BE of Ti 2p and lower BE of Fe 2p as obtained from XPS results. Thus in the TiO<sub>2</sub>@PCN-222-Fe heterojunction the Fermi level of TiO<sub>2</sub> decreased and the Fermi level of PCN-222-Fe increased; a unified Fermi level (−3.6 eV) in the TiO<sub>2</sub>@PCN-222-Fe heterojunction is formed between the two. Due to the difference in the Fermi levels, TiO<sub>2</sub> loses electrons and PCN-222-Fe gains electrons, thus bending up for TiO<sub>2</sub> and bending down for PCN-222-Fe at the interface of the two are formed. L-Cysteine in the interface of the two also plays the same role; −COO<sup>−</sup> coordinated with Ti<sup>4+</sup> shows the electron withdrawing effect and causes bending-up of TiO<sub>2</sub>, and −S<sup>−</sup> coordinated with Fe<sup>3+</sup> shows the electron donating effect and causes bending-down of PCN-222-Fe. These effects result in the L-cysteine side near TiO<sub>2</sub> becoming negatively charged and the L-cysteine side near PCN-222-Fe becoming positively charged, and an electric field is built. Thus bending-up of TiO<sub>2</sub> and bending-down of PCN-222-Fe formed the desired Z-scheme heterojunction as shown in Fig. 9c. Consequently, through L-cysteine coordination in the TiO<sub>2</sub>@PCN-222-Fe heterojunction, the photogenerated electrons in the bending down CB of PCN-222-Fe can easily recombine with

the photogenerated holes in the bending up VB of TiO<sub>2</sub>; the electrons remaining in the CB of TiO<sub>2</sub> act as the active site for CO<sub>2</sub> reduction and the holes remaining in the VB of PCN-222-Fe act as the active site for H<sub>2</sub>O oxidation. The Z-scheme structure results in a greatly enhanced separation efficiency of photogenerated carriers. Additionally, after the photocatalyst is excited by light, the electrons in the VB absorbed the photons and are excited to the CB, and holes are formed in the VB. The electrons in the CB and holes in the VB will recombine promptly to produce fluorescence, so the fluorescence intensity can effectively reflect the carrier separation efficiency. As can be seen from Fig. 8e and Fig. S14 (ESI<sup>†</sup>), fluorescence emission spectra of TiO<sub>2</sub> and PCN-222-Fe have partial overlap; pure TiO<sub>2</sub> exhibits strong PL intensity at about 385 nm and pure PCN-222-Fe exhibits relatively lower PL intensity at about 470 nm. The PL wavelength of TiO<sub>2</sub> (385 nm) is in good accordance with the band gap (3.29 eV) obtained from UV-vis spectra as shown in Fig. 9a. The fluorescence intensity of TiO<sub>2</sub>@PCN-222-Fe is reduced compared to that of pure PCN-222-Fe (the mass ratio of TiO<sub>2</sub>/PCN-222-Fe is 1/4), revealing that the combination of TiO<sub>2</sub> and PCN-222-Fe with L-cysteine can inhibit the recombination of photogenerated electrons and holes, thereby improving the photocatalytic activity. The average PL lifetime is generally considered to be a rough indicator of the separation efficiency of the light-excited carriers. In this regard, time-resolved PL detection was employed (Fig. 8f and Table S4, ESI<sup>†</sup>). The lifetime of

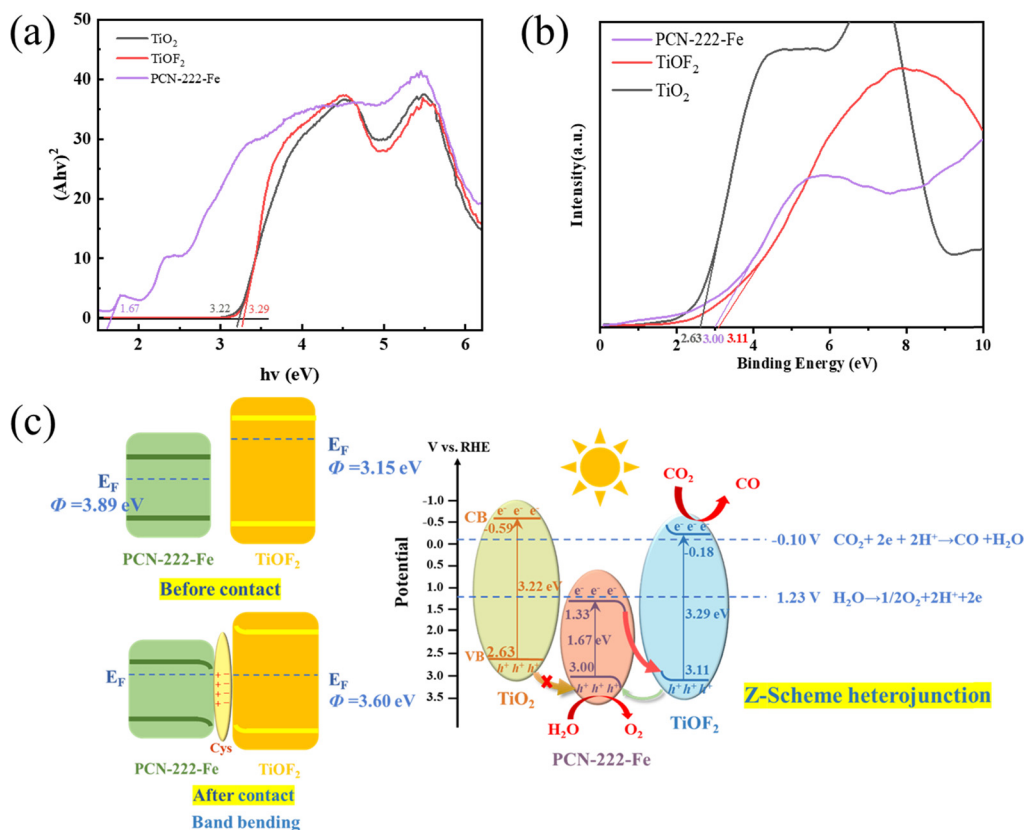


Fig. 9 (a) Tauc plots of TiO<sub>2</sub>, TiOF<sub>2</sub> and PCN-222-Fe. (b) XPS valence band spectra of TiO<sub>2</sub>, TiOF<sub>2</sub> and PCN-222-Fe. (c) Energy-level diagrams showing the electron transfer of TiO<sub>2</sub>@PCN-222-Fe.

TiOF<sub>2</sub>@PCN-222-Fe is extended to 2.04 ns compared with that of pure PCN-222-Fe (1.77 ns) and is near to that of TiOF<sub>2</sub> (2.12 ns), which further confirmed the efficient light-induced carrier separation for the heterojunction. The reduced PL intensity and the increased PL lifetime can be explained by the Z-scheme as described in Fig. 9c. The photogenerated electrons in the CB of bending-down PCN-222-Fe and the photogenerated holes in the VB of bending-up TiOF<sub>2</sub> recombined, and thus the remaining electrons in the CB of bending-up TiOF<sub>2</sub> and the remaining holes in the VB of bending-down PCN-222-Fe possess a long life time.

To further demonstrate the Z-scheme band structure of TiOF<sub>2</sub>@PCN-222-Fe for the visible light photocatalytic CO<sub>2</sub>RR, UV-vis diffuse reflectance spectroscopy was conducted (Fig. 4 and Fig. S5, ESI<sup>†</sup>) and the Tauc plot is shown in Fig. 9a; the absorption edge of TiOF<sub>2</sub> is slightly blue-shifted compared to that of TiO<sub>2</sub>, indicating that TiOF<sub>2</sub> has a wider band gap ( $E_g$ ) than TiO<sub>2</sub> due to the electron-withdrawing effect of fluorine. The band gaps of TiO<sub>2</sub>, TiOF<sub>2</sub> and PCN-222-Fe are calculated from the Tauc plot to be 3.22, 3.29 and 1.67 eV, respectively. PCN-222-Fe has a narrow band gap of 1.67 eV, which can absorb the visible light with low energy. It can be observed from Fig. 9b that the VB of TiO<sub>2</sub>, TiOF<sub>2</sub> and PCN-222-Fe is 2.63, 3.11 and 3.00 V vs. RHE, respectively. According to the  $E_g$  obtained above, the CB of TiO<sub>2</sub>, TiOF<sub>2</sub> and PCN-222-Fe is calculated to be -0.59, -0.18 and 1.33 V vs. RHE, respectively, as shown in Fig. 9c. The VB of pure TiOF<sub>2</sub> is much lower than that of pure TiO<sub>2</sub>, confirming that the electron-withdrawing effect of fluorine lowered the VB of TiOF<sub>2</sub>. In the TiOF<sub>2</sub>@PCN-222-Fe composite, the CB of TiOF<sub>2</sub> is much higher than the CB of PCN-222-Fe and the half-reaction potential for the reduction of CO<sub>2</sub> to CO (CO<sub>2</sub> + 2e + 2H<sup>+</sup> → CO + H<sub>2</sub>O, -0.10 V vs. RHE), indicating the CB of TiOF<sub>2</sub> possesses higher energetic electrons, which act as the active sites for the reduction of CO<sub>2</sub> to CO. The VBs in the TiOF<sub>2</sub>@PCN-222-Fe heterojunction decreased in the order of TiO<sub>2</sub> > PCN-222-Fe > TiOF<sub>2</sub> and all VBs are much lower than the half-reaction potential of the OER (H<sub>2</sub>O → 1/2O<sub>2</sub> + 2H<sup>+</sup> + 2e, 1.23 V vs. RHE), indicating that the photogenerated holes in the VB possess high energy and can oxidize H<sub>2</sub>O to O<sub>2</sub>. PCN-222-Fe shows the highest OER activity as shown in Fig. 7c and the holes in the VB of PCN-222-Fe are suggested to act as the active sites of the OER. The Z-scheme of the TiOF<sub>2</sub>@PCN-222-Fe heterojunction promotes the separation of electron-hole pairs, which meets the kinetic demands of the visible light photocatalytic CO<sub>2</sub> reduction to CO. The differences in the VBs of pure TiO<sub>2</sub>, TiOF<sub>2</sub> and PCN-222-Fe were also determined by UPS results (Fig. S15, ESI<sup>†</sup>). The yellow lines mark the baseline and tangent of the curves. The VBs of TiO<sub>2</sub>, TiOF<sub>2</sub> and PCN-222-Fe are calculated to be 2.7, 3.11 and 3.00 eV, which are consistent with the results obtained from XPS. The VB of pure TiOF<sub>2</sub> is much lower than that of pure TiO<sub>2</sub>, and the VB of pure PCN-222-Fe lies between the two. The lower the VB is, the higher the energy of photogenerated holes is. This result indicates that the photogenerated holes in the VB of TiOF<sub>2</sub> can transfer to the VB of PCN-222-Fe, while the photogenerated holes in the VB of TiO<sub>2</sub> cannot transfer to the VB of PCN-222-Fe. The difference in the VBs is the internal driving force of photogenerated hole

transfer for the TiOF<sub>2</sub>@PCN-222-Fe heterojunction, and the photogenerated holes concentrated on the VB of PCN-222-Fe can oxidize H<sub>2</sub>O to produce O<sub>2</sub>.

Based on the above characterization and visible light photocatalytic performance, the possible Z-scheme heterojunction is formed in TiOF<sub>2</sub>@PCN-222-Fe. The CO<sub>2</sub> photocatalytic reduction mechanism and electron-hole separation mechanism are shown in Fig. 9c. When irradiated with a Xe lamp emitting visible light, the electrons in the VBs of both PCN-222-Fe and TiOF<sub>2</sub> absorb the energy of visible light photons and are excited to the CBs and leave the holes in the VBs. Due to the electron-withdrawing effect of the -COO<sup>-</sup> group coordinated with Ti<sup>4+</sup>, the TiOF<sub>2</sub> interface would generate a bending-up energy level;<sup>43</sup> the energy barrier prevents the photogenerated electrons in the CB of TiOF<sub>2</sub> from migrating, thus prolonging the fluorescence lifetime. On the other hand, due to the electron-donating effect of the -S<sup>-</sup> group coordinated with Fe<sup>3+</sup>, the PCN-222-Fe interface would generate a bending-down energy level, and thus the photogenerated electrons in the CB of PCN-222-Fe can easily migrate to the VB of TiOF<sub>2</sub> to recombine with the photogenerated holes, indicating the Z-scheme structure of the heterojunction. Thus, the photogenerated electrons remaining in the CB of TiOF<sub>2</sub> can reduce CO<sub>2</sub> to CO, and the photogenerated holes remaining in the VB of PCN-222-Fe can oxidize H<sub>2</sub>O to O<sub>2</sub>. The photogenerated electrons and holes are effectively separated by the Z-scheme heterojunction. Moreover, photogenerated holes in the VB of TiOF<sub>2</sub> can also transfer to the VB of PCN-222-Fe, leading to higher amounts of holes on the VB of PCN-222-Fe acting as the active sites of the OER. While due to the VB of TiO<sub>2</sub> being higher than the VB of PCN-222-Fe, the energy of photogenerated holes in the VB of TiO<sub>2</sub> is lower and hence the holes cannot transfer to the VB of PCN-222-Fe. Thus, the TiOF<sub>2</sub>-based heterojunction possessed a higher CO<sub>2</sub>RR visible light photocatalytic activity than the TiO<sub>2</sub>-based heterojunction. In summary, the matched energy level structure and the interface band bending of the TiOF<sub>2</sub>@PCN-222-Fe heterojunction bonded with L-cysteine theoretically make it a potential catalyst for visible light CO<sub>2</sub> photoreduction, in which trace amounts of H<sub>2</sub>O can act as a hole sacrificial agent through the OER to assist in the reduction of CO<sub>2</sub>.

To further illustrate how the electric field formed in the TiOF<sub>2</sub>@PCN-222-Fe heterojunction facilitates the proton transportation, the zeta potential of pure TiOF<sub>2</sub>, pure PCN-222-Fe and the TiOF<sub>2</sub>@PCN-222-Fe heterojunction was used to test the ionic charge on the surface of the nanoparticles. It is clear that the zeta potential of pure TiOF<sub>2</sub> was approximately -2.10 mV, indicating that the surface of pure TiOF<sub>2</sub> nanoparticles exhibits a negative charge. For pure PCN-222-Fe, the zeta potential was high as 41.0 mV, indicating that the surface of pure PCN-222-Fe nanoparticles is positively charged. When the two are combined together with L-cysteine, it is noticeable that the zeta potential of TiOF<sub>2</sub>@PCN-222-Fe is 19.8 mV, between those of pure TiOF<sub>2</sub> and pure PCN-222-Fe. This is due to the electron-withdrawing effect of the -COO<sup>-</sup> group in L-cysteine attached with TiOF<sub>2</sub>; the negative charge of TiOF<sub>2</sub> nanoparticles at the interface of TiOF<sub>2</sub>@PCN-222-Fe is partially neutralized. Due to the electron-donating effect of

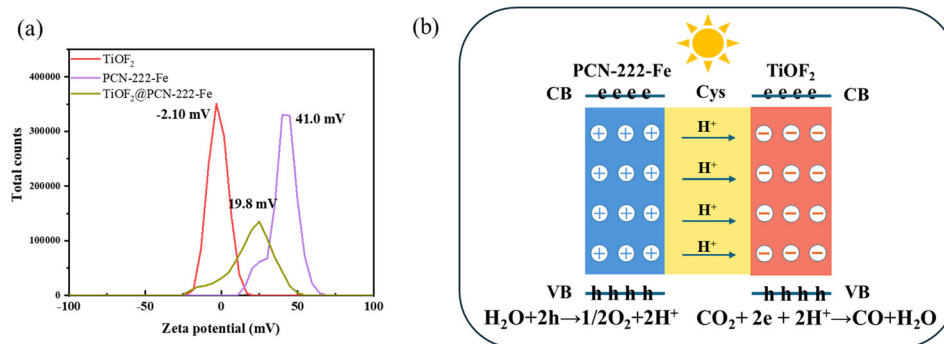


Fig. 10 (a) Zeta potentials of TiOF<sub>2</sub>, PCN-222-Fe and TiOF<sub>2</sub>@PCN-222-Fe. (b) Electric field distribution of TiOF<sub>2</sub>@PCN-222-Fe for proton transportation.

the  $\text{S}^-$  group in *L*-cysteine axially attached to  $\text{Fe}^{3+}$  in PCN-222-Fe, the positive charge of PCN-222-Fe nanoparticles at the interface of TiOF<sub>2</sub>@PCN-222-Fe is partially neutralized. Thus the zeta potential of TiOF<sub>2</sub>@PCN-222-Fe is between the two, and an electric field for the proton transportation is formed from PCN-222-Fe to TiOF<sub>2</sub>. In summary, as shown in Fig. 9c and 10b, the photogenerated electrons in the CB of PCN-222-Fe and the photogenerated holes in the VB of TiOF<sub>2</sub> recombined through the Z-scheme TiOF<sub>2</sub>@PCN-222-Fe heterojunction. The  $\text{-COO}^-$  group coordinated with bending up TiOF<sub>2</sub> can accumulate photogenerated electrons in the CB to reduce CO<sub>2</sub>. The  $\text{-S}^-$  group coordinated with bending down PCN-222-Fe can accumulate photogenerated holes in the VB to oxidize H<sub>2</sub>O. The lifetimes of photogenerated carriers are thus prolonged by the Z-scheme structure as shown in Fig. 8f and Table S4 (ESI<sup>†</sup>). The electric field from PCN-222-Fe nanoparticles to TiOF<sub>2</sub> nanoparticles as obtained from zeta potential measurements is conducive to proton transport.<sup>44</sup> The produced protons in the OER on the side of PCN-222-Fe can more easily transfer through *L*-cysteine to the side of TiOF<sub>2</sub> for the reduction of CO<sub>2</sub>, which can be explained by the increased amount of  $\text{-OH}$  hydroxyl groups in the TiOF<sub>2</sub>@PCN-222-Fe heterojunction as shown in Table S3 (ESI<sup>†</sup>). Consequently, the Z-scheme structure, the electric field and the agglomerant *L*-cysteine can all effectively modulate the charge separation and the proton transfer like cytochrome *c* oxidase, which in turn promotes the CO<sub>2</sub>RR and the OER processes.

#### 2.4. DFT calculations for determining the mechanism of CO<sub>2</sub> reduction

In order to further explain the mechanism of the high CO yield of TiOF<sub>2</sub>@PCN-222-Fe, a photocatalytic CO<sub>2</sub> reduction pathway was constructed by DFT calculations. As discussed above, the holes in the VB of PCN-222-Fe act as the active sites of the OER and the electrons in the CB of TiOF<sub>2</sub> act as the active sites of the CO<sub>2</sub>RR. Thus, the relative Gibbs free energies of TiO<sub>2</sub> and TiOF<sub>2</sub> for CO<sub>2</sub> reduction are calculated and the corresponding intermediate models are shown in Fig. 11. It is important to note that the transformation of excited  $\text{*CO}_2$  into  $\text{*COOH}$  is a rate determining step of the CO<sub>2</sub>RR, and this  $\text{*COOH}$  species intensified with the irradiation time, suggesting a sustained proton-assisted CO<sub>2</sub>RR. TiOF<sub>2</sub> requires a much lower Gibbs free energy for the transformation of  $\text{*CO}_2$  into  $\text{*COOH}$  as compared to TiO<sub>2</sub>, indicating that the protonation of excited  $\text{*CO}_2$  into  $\text{COOH}^*$  on TiOF<sub>2</sub> is much easier than that on TiO<sub>2</sub>. This result can be explained by the electron-withdrawing effect of the F element. Although  $\text{*COOH}$  to  $\text{CO}^*$  conversion requires a slightly higher Gibbs free energy for TiOF<sub>2</sub> than that for TiO<sub>2</sub>, TiOF<sub>2</sub> allows for an easier conversion of CO<sub>2</sub> to CO(g) for a more thermodynamically advantageous process, which favors higher CO yields for TiOF<sub>2</sub>@PCN-222-Fe heterostructures. Due to that, TiOF<sub>2</sub> has a lower Gibbs free energy compared to TiO<sub>2</sub>; the TiOF<sub>2</sub>-based heterojunction shows a higher photocatalytic performance and faster charge transfer than the TiO<sub>2</sub>-based heterostructure.

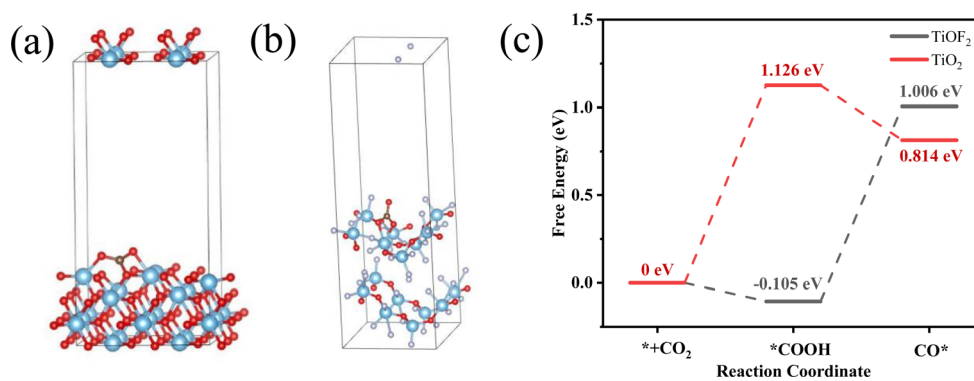


Fig. 11 The DFT calculation and proposed reaction mechanism. The optimized geometries of CO<sub>2</sub> adsorbed on the (001) surface of TiO<sub>2</sub> (a) and TiOF<sub>2</sub> (b). (c) Calculated Gibbs free energy profile.

### 3. Conclusions

In summary, TiOF<sub>2</sub> nanoparticles successfully agglomerated with PCN-222-Fe nanoparticles through self-assembled L-cysteine. The -SH group in L-cysteine axially coordinated with Fe<sup>3+</sup> in PCN-222-Fe and had an electron-donating effect on Fe<sup>3+</sup>. The -COOH group in L-cysteine coordinated with TiOF<sub>2</sub> and had an electron-withdrawing effect on Ti<sup>4+</sup>. The CB of TiOF<sub>2</sub> is higher than the CB of PCN-222-Fe and the VB of TiOF<sub>2</sub> is lower than the VB of PCN-222-Fe; the Z-scheme heterojunction and band bending were observed by investigating the Fermi level through UPS characterization, which were conducive to separating photogenerated carriers. The electrons on the CB of PCN-222-Fe and the holes on the VB of TiOF<sub>2</sub> recombined; the electrons on the CB of TiOF<sub>2</sub> remained for CO<sub>2</sub> reduction and the holes on the VB of PCN-222-Fe remained for H<sub>2</sub>O oxidation. An electric field from PCN-222-Fe to TiOF<sub>2</sub> is formed and characterized by zeta potential measurements, which is conducive to the proton transfer from PCN-222-Fe to TiOF<sub>2</sub> through the L-cysteine agglomerant. The TiOF<sub>2</sub>@PCN-222-Fe heterojunction was found to exhibit high catalytic activity in the CO<sub>2</sub>RR and OER. The yield of CO was 6.72 μmol g<sup>-1</sup>, which was better than those of many MOF-based and TiO<sub>2</sub>-based photocatalysts. The axially coordinated ferroporphyrin center acts as the active site of the OER, and TiOF<sub>2</sub> act as the active site of CO<sub>2</sub> reduction in the TiOF<sub>2</sub>@PCN-222-Fe heterojunction. The high visible light photocatalytic performance of TiOF<sub>2</sub>@PCN-222-Fe can be attributed to the enhanced photocurrent, conductivity, the electric field, the Z-scheme and the self-assembled L-cysteine, all of which can effectively modulate carrier separation and proton transfer like cytochrome *c* oxidase. DFT calculations also indicate that the protonation of excited \*CO<sub>2</sub> into COOH\* on TiOF<sub>2</sub> is much easier than that on TiO<sub>2</sub>. This study provides a new biomimetic strategy for effectively promoting CO<sub>2</sub> photoreduction. The L-cysteine agglomerant is expected to be applied to the synthesis of other heterojunctions. TiOF<sub>2</sub> shows a lower VB with energetic holes than TiO<sub>2</sub>, which is also expected to achieve efficient photoactivity for various other photocatalysis reactions.

### Author contributions

Yi Ping: investigation, formal analysis, visualization, writing – original draft, validation; Chuan-Jiao Wang: investigation, formal analysis, visualization; Chang-An Hou: investigation, validation; Zhen-Feng Shang: writing – reviewing and editing; and Dan-Hong Wang: writing – reviewing and editing, project administration, funding acquisition.

### Data availability

The data supporting this article have been included as part of the ESI.†

### Conflicts of interest

There are no conflicts to declare.

### Acknowledgements

This work was supported by the National Natural Science Foundation of China (22372082) and the 111 project (B18030) from China. The authors also acknowledge the financial support of the Haihe Laboratory of Sustainable Chemical Transformations (YYJC202101) and the National Key Research and Development Program of China (2022YFA1502901).

### Notes and references

- 1 X. Bi, Y. Yan, H. Wang, Y. Zhao, J. Zhang and M. Wu, *Energy Mater. Adv.*, 2023, **4**, 0037.
- 2 K. Niu, Y. Xu, H. Wang, R. Ye, H. L. Xin, F. Lin, C. Tian, Y. Lum, K. C. Bustillo, M. M. Doeff, M. T. M. Koper, J. Ager, R. Xu and H. Zheng, *Sci. Adv.*, 2017, **3**, e1700921.
- 3 W. Ye, Y. Wang, G. Ji, F. Zhang, Y. Zhao and Z. Liu, *ChemSusChem*, 2022, **15**, e202200759.
- 4 C. Liao, K. Yamauchi and K. Sakai, *ACS Catal.*, 2024, **14**, 11131–11137.
- 5 M. Zhang, Y. Mao, X. Bao, P. Wang, Y. Liu, Z. Zheng, H. Cheng, Y. Dai, Z. Wang and B. Huang, *ACS Catal.*, 2024, **14**, 5275–5285.
- 6 X. Sun, L. Li, S. Jin, W. Shao, H. Wang, X. Zhang and Y. Xie, *eScience*, 2023, **3**(2), 100095.
- 7 B. Song, Y. Liang, Y. Zhou, L. Zhang, H. Li, N.-X. Zhu, B. Z. Tang, D. Zhao and B. Liu, *J. Am. Chem. Soc.*, 2024, **146**, 14835–14843.
- 8 S. Cong, Y. Zhou, C. Luo, C. Wang, J. Wang, Z. Wang and X. Liu, *Angew. Chem., Int. Ed.*, 2024, **63**, e202319894.
- 9 Z.-B. Fang, T.-T. Liu, J. Liu, S. Jin, X.-P. Wu, X.-Q. Gong, K. Wang, Q. Yin, T.-F. Liu, R. Cao and H.-C. Zhou, *J. Am. Chem. Soc.*, 2020, **142**, 12515–12523.
- 10 X. Feng, Y. Pi, Y. Song, C. Brzezinski, Z. Xu, Z. Li and W. Lin, *J. Am. Chem. Soc.*, 2020, **142**, 690–695.
- 11 Q. Huang, J. Liu, L. Feng, Q. Wang, W. Guan, L.-Z. Dong, L. Zhang, L.-K. Yan, Y.-Q. Lan and H.-C. Zhou, *Nat. Sci. Rev.*, 2020, **7**, 53–63.
- 12 D. Feng, Z.-Y. Gu, J.-R. Li, H.-L. Jiang, Z. Wei and H.-C. Zhou, *Angew. Chem., Int. Ed.*, 2012, **51**, 10307–10310.
- 13 Q. Huang, Q. Niu, X.-F. Li, J. Liu, S.-N. Sun, L.-Z. Dong, S.-L. Li, Y.-P. Cai and Y.-Q. Lan, *Sci. Adv.*, 2022, **8**, eadd5598.
- 14 Y. Feng, Y. Zhang, J. Wang, L. Ling, R. Zhang, M. Fan, B. Hou, D. Li and B. Wang, *ACS Catal.*, 2024, **14**, 1874–1881.
- 15 J. Wang, F. Cao, Z. Bian, M. K. H. Leung and H. Li, *Nanoscale*, 2014, **6**, 897–902.
- 16 Q. Li, C. Wang, H. Wang, J. Chen, J. Chen and H. Jia, *Angew. Chem., Int. Ed.*, 2024, **63**, e202318166.
- 17 J. Chen and W. Xu, *eScience*, 2023, **3**(6), 100178.
- 18 Z. Zhang, K. Xiang, H. Wang, X. Li, J. Zou, G. Liang and J. Jiang, *SusMat*, 2024, **4**, e229.
- 19 C. Hou and X. Kong, *Huagong Huanbao*, 2022, **42**(2), 203–209.
- 20 C. Li, Z. Wang, L. Wang, Q. Bai, B. Wang and C. Hao, *J. Mol. Liq.*, 2022, **366**, 120335.

- 21 S. Wang, L. Pan, J.-J. Song, W. Mi, J.-J. Zou, L. Wang and X. Zhang, *J. Am. Chem. Soc.*, 2015, **137**, 2975–2983.
- 22 P. Dong, E. Cui, G. Hou, R. Guan and Q. Zhang, *Mater. Lett.*, 2015, **143**, 20–23.
- 23 A. T. Stoltzfus, J. G. Ballot, T. Vignane, H. Li, L. Muller, M. A. Siegler, M. A. Kane, M. R. Filipovic, D. P. Goldberg and S. L. J. Michel, *Angew. Chem., Int. Ed.*, 2024, **63**, e202401003.
- 24 J.-X. Xiao, F.-X. Li, S.-J. Ren and J. Qu, *Angew. Chem., Int. Ed.*, 2024, **63**, e202403597.
- 25 L. Zhao, X. Zhao, W. Zhang, Y. Miao, X. Wang and D. Deng, *Adv. Funct. Mater.*, 2024, 2404789.
- 26 Q. Liu, Y. Yu and H. Wang, *J. Nat. Sci. Heilongjiang Univ.*, 2015, **32**, 360–365.
- 27 J. Wu, X. Zhao, Y. Zou, X. Wu, W. Bai and X. Zeng, *Microchem. J.*, 2021, **164**, 105952.
- 28 X. Huang and J. T. Groves, *Chem. Rev.*, 2018, **118**, 2491–2553.
- 29 M. Wikström, K. Krab and V. Sharma, *Chem. Rev.*, 2018, **118**, 2469–2490.
- 30 P. M. Usov, S. R. Ahrenholtz, W. A. Maza, B. Stratakes, C. C. Epley, M. C. Kessinger, J. Zhu and A. J. Morris, *J. Mater. Chem. A*, 2016, **4**, 16818–16823.
- 31 J. Sun, H. Yin, P. Liu, Y. Wang, X. Yao, Z. Tang and H. Zhao, *Chem. Sci.*, 2016, **7**, 5640–5646.
- 32 Y. Han, Y. Wu, W. Lai and R. Cao, *Inorg. Chem.*, 2015, **54**, 5604–5613.
- 33 D. Wang and J. Groves, *Proc. Natl. Acad. Sci. U. S. A.*, 2013, **110**(39), 15579–15584.
- 34 X. Wang, Z.-F. Cai, D. Wang and L.-J. Wan, *J. Am. Chem. Soc.*, 2019, **141**, 7665–7669.
- 35 Y. Liu, Y. Han, Z. Zhang, W. Zhang, W. Lai, Y. Wang and R. Cao, *Chem. Sci.*, 2019, **10**, 2613–2622.
- 36 K. Nakamoto, *Infrared and Raman Spectra of Inorganic and Coordination Compounds*.
- 37 S. Choi, T. G. Spiro, K. C. Langry, K. M. Smith, D. L. Budd and G. N. La Mar, *J. Am. Chem. Soc.*, 1982, **104**, 4345–4351.
- 38 S. Choi, T. G. Spiro, K. C. Langry and K. M. Smith, *J. Am. Chem. Soc.*, 1982, **104**, 4337–4344.
- 39 S. Hu and T. Jiang, *Chin. J. Chem. Phys.*, 1992, **5**(4), 286–291.
- 40 C. Wang, S. Wang, Y. Ping, Z. Zhao, D. Guo, D. Wang and X. Bu, *Appl. Catal., B*, 2024, **347**, 123781.
- 41 S. Huang, T. Ouyang, B. Zheng, M. Dan and Z. Liu, *Angew. Chem., Int. Ed.*, 2021, **60**, 9546–9552.
- 42 H. Yu, F. Chen, X. Li, H. Huang, Q. Zhang, S. Su, K. Wang, E. Mao, B. Mei, G. Mul, T. Ma and Y. Zhang, *Nat. Commun.*, 2021, **12**, 4594.
- 43 X. Li, Q. Dong, F. Li, Q. Zhu, Q. Tian, L. Tian, Y. Zhu, M. Padervand and C. Wang, *Appl. Catal., B*, 2024, **340**, 123238.
- 44 Z. Ding, S. Wang, X. Chang, D.-H. Wang and T. Zhang, *RSC Adv.*, 2020, **10**, 26246–26255.